ACS NANO
Cite This: ACS Nano 2018, 12, 4321−4337
www.acsnano.org

ARTICLE

Self-Assembly of Ionic Microgels Driven by an Alternating Electric Field: Theory, Simulations, and Experiments

Thiago Colla,[†,‡] Priti S. Mohanty,[∥,§] Sofi Nöjd,[∥] Erik Bialik,[∥] Aaron Riede,[∥] Peter Schurtenberger,[∥] and Christos N. Likos*[,‡]

[†]Instituto de Física, Universidade Federal de Ouro Preto, CEP 35400-000 Ouro Preto, Minas Gerais, Brazil
[‡]Faculty of Physics, University of Vienna, Boltzmanngasse 5, 1090 Vienna, Austria
[∥]Division of Physical Chemistry, Lund University, SE-221 00 Lund, Sweden
[§]School of Chemical Technology, Kalinga Institute of Industrial Technology (KIIT), Bhubaneswar 751024, India

ABSTRACT: **The structural properties of a system of ionic microgels under the influence of an alternating electric field are investigated both theoretically and experimentally. This combined investigation aims to shed light on the structural transitions that can be induced by changing either the driving frequency or the strength of the applied field, which range from string-like formation along the field to crystal-like structures across the orthogonal plane. In order to highlight the physical mechanisms responsible for the observed particle self-assembly, we develop a coarse-grained description, in which effective interactions among the charged microgels are induced by both equilibrium ionic distributions and their time-averaged hydrodynamic responses to the applied field. These contributions are modeled by the buildup of an effective dipole moment at the microgels backbones, which is partially screened by their ionic double layer. We show that this description is able to capture the structural properties of this system, allowing for very good agreement with the experimental results. The model coarse-graining parameters are indirectly obtained *via* the measured pair distribution functions and then further assigned with a clear physical interpretation, allowing us to highlight the main physical mechanisms accounting for the observed self-assembly behavior.**

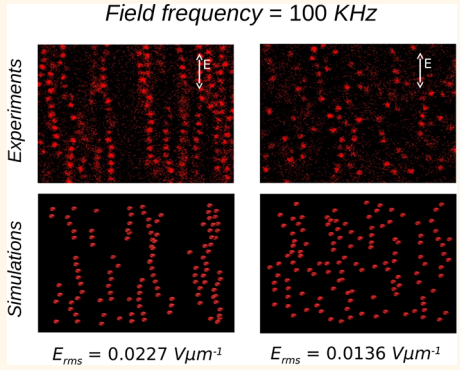

KEYWORDS: *soft colloids, ionic microgels, self-assembly, dipoles, coarse-graining, confocal microscopy, chain formation*

Soft nanoparticles are known to act as prototypical building blocks for the manufacturing of smart responsive materials with controllable features.[1−5] There are many different approaches to experimentally trigger the self-assembly of these nanoparticles, in such a way as to target desirable macroscopic structures with tunable properties.[6,7] The general strategies usually go along the lines of controlling effective interactions by adjusting the synthesis mechanisms and/or the properties of the environment the particles are embedded into, in such a way as to manipulate their dynamical and structural equilibrium assemblies. In this respect, biological systems provide excellent templates to nanoparticle self-assembly both in bulk[8−15] and in interfacial[14,16,17] environments. In this case, however, the interactions and physical mechanisms responsible for particle aggregation are generally quite complex and difficult to reproduce.[8] In practical applications, on the other hand, it is usually desirable to design simple systems which are yet able to assemble into complex structures in a controllable way.

Several inherent properties of nanoparticles such as their size, shape, charge, and degree of polydispersity can be reasonably well controlled during the synthesis mechanisms to render particles a rich variety of interactions and self-assembly properties.[7,18,19] Decorating nanoparticles with asymmetric patches,[20−26] coating them with different objects,[27−29] or grafting polymer chains along their surfaces[30−33] are among the usual synthesis protocols adopted to achieve desirable particle effective interactions in the case of hard surfaces.[3,34] In soft nanoparticles, the degree of softness and the size/shape deformations under external stress are essential features to control their equilibrium properties with the environment.[35−40] Solvent properties such as pH, permittivity, and solvent quality can also have a strong influence on the way suspended nanoparticles interact with one another.[41−46] Furthermore, addition of components of smaller length scales such as

Received: December 14, 2017
Accepted: April 10, 2018
Published: April 10, 2018

© 2018 American Chemical Society

DOI: 10.1021/acsnano.7b08843
ACS Nano 2018, 12, 4321−4337

polymer chains or ionic components provides also a convenient route to properly tune desirable effective interactions.[34,47−49] In general, the more sensitive the particles are to such changes in their environmental conditions, the richer the class of mutual interactions and morphological properties that can be artificially induced upon them. In this sense, microgels (or nanogels in a smaller length scale) represent promising candidates for the design of responsive materials with well controllable behavior.[1,35,36,50,51] Contrary to hard nanoparticles, soft microgels are able to change their size and internal conformation in response to external stimuli, the equilibrium properties being mostly dictated by the osmotic flow across their interfaces.[52−57] The elastic character of the cross-linked polymer chains allows microgels to deform and partially interpenatrate each other whenever strong attractive forces among them are present.[58−60] This also makes it possible to assemble these particles into very compact aggregates or even synthesizing them at local volume fractions that exceed close-packing,[60] considerably changing the overall self-assembly scenario with respect to hard particle iterations.

Aside from the aforementioned strategies to induce effective interactions, another possibility to steer nanoparticle self-assembly which has attracted a lot of attention over the past decade is by subjecting them to an external drive, such as suitably controlled electric or magnetic fields.[7,61−72] This technique has the clear advantage of being easily tunable to reach the desirable assembly scenario, as the response of nanoparticles to the applied field can be well tuned by either changing the system properties or by properly switching the field parameters.[7,62] In many situations, the external field can be controlled such as to drive the system to trapped structural configurations which will persist for long time scales even after the field has been switched off.[65] This possibility of directing the spatial system inhomogeneity *via* the application of an external field can be used to induce bulk particle conformations which would be otherwise very difficult to emerge spontaneously from particle interactions alone.

Quite recently, it has been shown in a series of works that a rich variety of self-assembly scenarios can be induced by submitting a system of ionic microgels to an alternating electric field.[61,64,65,73] The observed structural properties feature a string-fluid transition at moderate applied frequencies or the formation of long rigid chains along the field direction at smaller frequencies, which further assemble into ordered solid-like structures across the perpendicular plane.[64] Both the rich structural transitions and the dynamical properties of the particle aggregation have been extensively studied as a function of field strengths and frequency. Moreover, a recent study of the dielectric properties of this system has revealed the main mechanisms accounting for dielectric responses in different frequency domains.[73] Depending on the imposed frequency, different dominant contributions are responsible for the overall polarization, reflecting the characteristic length scales that are excited more intensively at different oscillation modes. In spite of the detailed analysis of the system response to the applied field, a theoretical model capable of describing the observed structural features in terms of the experimentally measured quantities is up to now still missing.

From a theoretical perspective, a comprehensive description of self-assembling processes in soft matter systems in terms of experimentally controllable parameters is a rather challenging task.[34,48] In spite of the huge progress in computational power acquired over the past decades, a proper description accounting for all relevant contributions is in most cases computationally unfeasible, since the different components have time and length scales which typically differ from one another by orders of magnitude. The conventional way of circumventing this drawback is to rely on coarse-graining approaches, in which some of these contributions are averaged out and collected altogether into effective parameters.[34,74] The connection between such coarse-graining parameters and the quantities typically accessible to experiments is not always clear, and a great deal of physical insight is sometimes required to properly interpret experimental data based on such model parameters. One typical limitation in trying to match experimental data by means of coarse-graining approaches is that they usually require some degree of approximation (*e.g.*, neglecting many-body interactions, mean-field, linear-like, or infinite dilution approximations) to be invoked in order to end up with numerically tractable situations. To what extent such approximations are able to reproduce real systems properties depends primarily on the specific experimental conditions at hand. A usual approach is to use effective quantities as fitting parameters to reproduce the measured data and then to assign them a proper physical interpretation based on the particular model system.

The Physics of Field-Induced Chain Aggregation. It is well-known that the application of suited external electric or magnetic fields in a number of systems of suspended nanoparticles gives rise to string-like formations along the field direction. In general terms, the origins of this phenomenon of chain aggregation can be traced back to field-induced, attractive dipole−dipole interactions. The physical mechanisms that ultimately lead to such induced dipole attraction along the field direction depend, on the other hand, on the specific coupling between particle system and applied field. In the case of ferrofluids (or magnetic colloids) subject to an external magnetic field, for example, it is the susceptibility mismatch between particles and solvent that triggers the field-induced dipole interactions (in addition to zero-field magnetic dipole interactions). A similar process is also known to induce dipole interactions in the case of hard colloids subject to an alternating electric field. In this case, it is the dielectric mismatch between colloids and solvent that gives rise to an effective dipole moment on these particles. The mechanism of field-induced interactions increases considerably in complexity in the case of charged colloids, since the external field will typically polarize the electric double layers, inducing effective dipole interactions which depend on the (hydrodynamic-driven) ionic response to the electric field. When nanoparticles are permeable to solvent molecules (as is the case of microgels or star polymers), the effects from dielectric mismatch on the underlying induced dipole moments can be in general neglected. The main mechanisms responsible for dipole interactions are, in this case, the responses of the counterions, both those condensed at the polymer backbones and those found at the double layer. The resulting dielectric spectra of this system become quite complex, since different frequency domains are characterized by the main influence of quite different ionic polarization mechanisms.[73,75]

From the point of view of theoretical developments, the description of chain aggregation in terms of induced dipole interactions goes back to the pioneering work of de Gennes and Pincus on the string formation in ferrofluids.[76] A number of similar approaches have been put forward to successfully describe the distribution and topology of particle aggregation in a number of magnetic fluids composed of both mono-[77−80] and

DOI: 10.1021/acsnano.7b08843
ACS Nano 2018, 12, 4321−4337

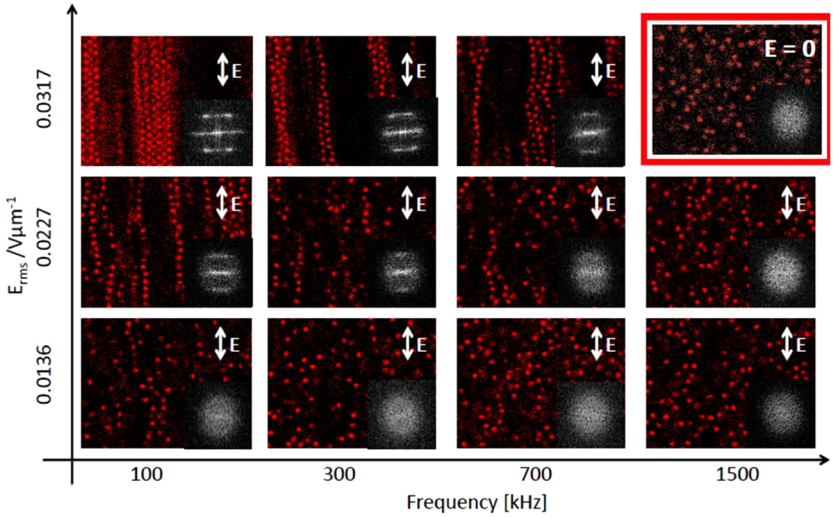

Figure 1. CLSM images of field-driven self-assembly of ionic microgels at an effective volume fraction of ϕ_{eff} = 0.1 in the swollen state (T = 20 °C) as a function of field strength E_{rms} and frequency f. Shown are 2D snapshots and an inset that depicts the Fourier transform of the corresponding image. Also shown is an image obtained with the suspension at zero field in the upper right corner.

polydisperse[81,82] magnetic particles. These density-functional-based approaches rely on the minimization of an approximate Helmholtz free energy which explicitly depends on the distribution of chains of a given size and topology (*e.g.*, chains or rings). Usually, a nearest-neighbor interaction approximation is invoked, allowing for simple numerically tractable approaches able of capturing several aspects of chain formation.[77,78,81] Other typical approaches to predict chain formation for a given effective dipole interaction are the Ornstein−Zernike integral equation approaches and computer simulations. The former is particularly useful to efficiently describe the onset of string-fluid formation, characterized by the divergence of the structure factor at a wavelength typical for particle aggregation. In the case of hard colloids, it is useful to adopt a model system in which a dipole electric/magnetic moment is embedded at the center of a hard sphere. In the case of charged colloids, this approximation leads to monopole interactions comprised by hard-sphere and Yukawa-like interactions, combined with a point dipole−dipole interaction. Although not as accurate as computer simulations, this approach is able to qualitatively capture many features of chain-like formation in these systems.[83]

An accurate description of field-induced dipole interactions in the case of ionic microgels requires, on the other hand, the use of more elaborated approaches. This is not only due to the complex dielectric response of these systems (which, in contrast to hard-sphere colloids, is not dominated by dielectric mismatch), but mainly because these particles are allowed to strongly interpenetrate one another. As a consequence, the approximation of unscreened point-like dipole interactions is in this case rather artificial, especially at the onset of chain formation when particles can considerably overlap each other, resulting in more complex dipole interactions. Moreover, the possibility of particle interpenetration should boost the emergence and growth of chain-like aggregates, as particles tend to bind closer together, forming more stable aggregates. A detailed description of the dipole interactions that lead to the experimentally observed chain formation in these systems is still lacking. The main goal of this work is to provide such a description by proposing a general coarse-graining approach able of incorporating the overall physical mechanisms of chain formation over the broad spectrum of frequency domains. The resulting effective interactions depend on coarse-graining parameters that can be readily interpreted in terms of underlying physical properties. Comparisons with experiments are performed up to the emergence of lateral chain−chain ordering, showing a quite good agreement that validates the underlying assumptions.

We shall here provide a combined experimental and theoretical analysis of the self-assembly of ionic microgels driven by an AC electric field. To this end, we will adopt a coarse-graining approach in which the overall effects from the time-dependent field are averaged out to provide an effective dipolar charge at each individual microgel. The time-averaged ionic response to the applied field is then described in this framework through anisotropic equilibrium ionic profiles resulting from the interactions with the microgel dipole charges. The ionic responses to both monopole and dipole fields are then worked out at the same linear level of approximation. While such linear approximation is only valid for not too strong microgel-ion interactions, its predictions for the ionic distributions are known to be accurate at distances beyond the ionic double layer, provided the effective parameters are properly renormalized to incorporate the nonlinearities present in this region.[34] Since we shall here compute these effective parameters directly from the measured data, we can consider them to be already the renormalized quantities that take into account nonlinear effects. Although treated at the same level of approximation, we will consider different degrees of ionic response to monopole and dipole contributions. The counterions condensed at the particle backbones do not screen the monopole interactions. So the major contributions from the monopole screening come only from the free ions present in the solution. These ions respond to the monopole field in such a way as to effectively screen these interactions. The (time-averaged) anisotropic distributions coupled to the dipole charges are proportionally weaker, resulting in a weaker screening of dipole interactions.[75,84] As we will see later on, this assumption is well justified over a large region of the dielectric spectra, whereby the oscillation period of the driving force is much shorter than the typical diffusion times of bulk ions.[73] By means of molecular dynamics (MD)

DOI: 10.1021/acsnano.7b08843
ACS Nano 2018, 12, 4321−4337

simulations and liquid-state integral equations (IE) techniques, the predictions of the model system are directly compared with experimental measurements for the in and out of plane pair correlation functions. A very good agreement is observed, which is later on probed by comparing the obtained effective dipole moments with the ones calculated from dielectric spectroscopy measurements for the same system, thereby validating the underlying theoretical assumptions and providing a robust and reliable description of driven self-assembly by means of time-averaged effective interactions arising from equilibrium considerations.

The remaining of this work is organized as follows. In the Results and Discussion section, the experimental system under investigation is presented in some detail, along with its synthesis protocol. The theoretical model considered to describe this system is subsequently outlined, followed by comparisons between experiments and theoretical predictions, which are critically discussed. A brief discussion on the numerical and experimental methods employed in this analysis is then provided in the Methods section. In the Conclusions section, some concluding remarks and perspectives for future investigations are outlined.

RESULTS AND DISCUSSION

Experimental Observations. We first describe the behavior of fully deionized microgel suspensions at low density (effective packing fraction $\phi_{eff} = 0.1$) in the swollen state (T = 20 °C) in the presence of an alternating electric field, which is applied in the image plane, with amplitude E_0 and angular frequency $\omega = 2\pi f$. The root-mean-square value $E_{rms} = E_0/\sqrt{2}$ is a convenient measure of the field strength. The particles used are almost monodisperse ionic poly-*N*-isopropylacrylamide (PNIPAM) microgels with a cross-link density of 5 mol % and a hydrodynamic radius of a_H = 530 nm, as determined by dynamic light scattering (see Methods and refs 64 and 65 for more details on the synthesis and particle characterization).

A summary of the overall field-driven assembly of microgel particles at different electric field strengths and frequencies is given in Figure 1, where 2D snapshots obtained by confocal laser scanning microscope (CLSM) are shown together with a Fourier transform of the corresponding images. The CLSM images obtained at a fixed frequency f = 100 kHz clearly demonstrate field-induced transitions with increasing field strength from E = 0 to E_{rms} = 0.0317 Vμm^{-1}. At low field strength, E_{rms} = 0.0136 Vμm^{-1}, the microgels slowly start to align along the field direction to form chains containing only two or three particles. At this low field strength, chains form and break spontaneously due to the competition between thermal energy and weak induced dipolar interactions. With increasing E, the chain length increases, and chains stiffen (see image at E_{rms} = 0.0227 Vμm^{-1}). At higher field strengths, E_{rms} = 0.0317 Vμm^{-1}, the chain length further grows, and the chains associate laterally, form aggregates, and subsequently crystallize into a body centered tetragonal structure (BCT). Details of the concentration-dependent field-induced phase behavior and the field-directed self-assembly can be found elsewhere.[64,65]

Interestingly, when keeping the field strength constant and varying the frequency from 100 kHz to 1500 kHz, the propensity of the microgels to self-assemble and form chains decreases, see Figure 1. This frequency dependence of the field-driven particle assembly can be understood from our recent dielectric spectroscopy study.[73] The dominant polarization mechanisms for ionic microgels in an external AC field are due to the mobility of internal counterions at low frequencies, the diffuse double layer around the particles at intermediate frequencies, and the polymer backbone at higher frequencies, that is, in the MHz regime. Moreover, the polymer backbone polarization is much weaker when compared to double layer and counterion polarization arising at low and intermediate frequencies, respectively.[73]

Based on our visual observations, two distinct regimes can be defined: (a) a weakly anisotropic regime at lower E_{rms} = 0.0136 Vμm^{-1}, where it is difficult to distinguish the structural changes that occur at different frequencies (bottom row in Figure 1), and (b) a strongly anisotropic regime at higher $E_{rms} \geq$ 0.0227 Vμm^{-1}, where long-range correlations in the form of particle association into chains along the field direction and weakening of these structures with increasing frequency are clearly visible (middle and top rows in Figure 1). While these observations provide a qualitative picture of the field-driven self-assembly of ionic microgels as a function of field strength and frequency, we will now develop a model that provides quantitative information on the radial distribution function $g(\mathbf{r})$ along and perpendicular to the electric field direction. Here we concentrate on the fluid-string regime at E_{rms} = 0.0136 Vμm^{-1} and 0.0227 Vμm^{-1}, respectively, where we compare our experimental data with predictions from theory and simulation.

Theory of Electric Field-Driven Effective Interactions. In order to theoretically describe the system outlined above, we consider a coarse-grained approach in which the effects from the AC field (time-averaged over one cycle) are modeled through the buildup of dipolar charges at the microgel boundaries aligned to the field, which can be further screened by the surrounding counterions. While these dipoles should qualitatively account for the field-induced microgel attraction along the field direction, the partial screening of these interactions represents (in a linear level) the time-averaged anisotropic ionic distribution caused by the AC field. In addition, the microgels carry a net, fixed monopole charge, see Figure 2a. We are going to employ a linearized Debye−Hückel approach to derive both monopole and dipole interactions for the experimental system outlined above. First, we will calculate monopole and dipole electric fields under the assumptions of static and time-averaged interactions, respectively. The resulting potentials will then be used to compute pair correlation functions for (decoupled) monopole−monopole and dipole−dipole interactions. Finally, these interactions will be combined with a short-ranged repulsion, which qualitatively accounts for the elastic repulsion under mutual compression to build-up a coarse-graining effective pair potential. The reader already familiar with the derivation of monopole interactions in charged microgels in this context can skip this first part or the coarse-graining potential derivation.

In the framework of a linear approximation for the ionic responses to both monopole and dipole microgel contributions, it can be readily shown that the effective Hamiltonian for the microgel system (after averaging out ionic contributions) comprises only zero and pairwise additive many-body contributions (known as volume terms and effective pair interactions, respectively). The former contributions are relevant for calculating thermodynamic properties, while the latter dictates the structural transitions whenever third- and higher-order body effects are negligible. The electrostatic contribution to the effective pair interactions at this linear level reads as

DOI: 10.1021/acsnano.7b08843
ACS Nano 2018, 12, 4321−4337

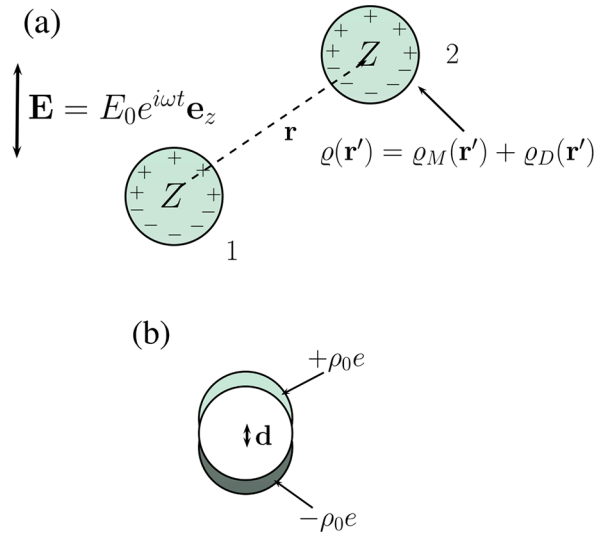

Figure 2. Sketch of our model system. (a) Microgels under the influence of an AC field of amplitude E_0 and frequency ω along the $\hat{\mathbf{e}}_z$ direction will acquire a frequency-dependent dipole charge $\varrho_D(\mathbf{r})$ in addition to the equilibrium monopole charge distribution $\varrho_M(\mathbf{r}) = 3Ze\Theta(a - r)/4\pi a^3$. (b) The dipolar-induced charges are obtained by overlapping two such oppositely charged monopoles with uniform charge distributions $\pm \rho_0 e$ up to a center-to-center distance d. The dipole charge distribution $\varrho_D(\mathbf{r}) = P\delta(a - r)\,\hat{\mathbf{e}}_r \cdot \hat{\mathbf{e}}_z$ follows by taking the limits $d \to 0$ and $\rho_0 \to \infty$, while keeping the product $P = \rho_0 ed$ constant. The microgel polarization points in the direction of the applied field, $\hat{\mathbf{e}}_z$.

$$u_{elec}(\mathbf{r}) = \int d\mathbf{r}'\psi(\mathbf{r}' - \mathbf{r})\varrho(\mathbf{r}') \tag{1}$$

where $\varrho(\mathbf{r}')$ is the charge distribution assigned to each microgel, and $\psi(\mathbf{r})$ is the ion-averaged potential around one microgel. As discussed above, the microgel charge distribution can be further split into monopole and dipole contributions, $\varrho(\mathbf{r}) = \varrho_M(\mathbf{r}) + \varrho_D(\mathbf{r})$. There are different possibilities of choosing a monopole charge distribution to reproduce the internal conformation of the charged polymer backbones. In the case loosely cross-linked microgels in a swollen state, a picture which is capable of capturing the essential system features in a simple way is that of a uniform charge distribution smeared out over the particle volume, $\varrho_M(\mathbf{r}) = 3Ze\Theta(a - r)/4\pi a^3$, where a is the microgel radius, e is the proton charge, and Z is the valency of the microgel (we have assumed positively charged microgels, without loss of generality). It might be argued that such a uniform charge density is a rather crude approximation to the real backbone charge distribution, which is (in view of the relatively large particle sizes) most likely of a core−shell nature. However, introduction of inhomogeneous monopole charge distributions at such a first-level approximation would only render the monopole interactions unnecessarily complex, without changing the physics behind the dipole interactions that lead to nontrivial particle self-assembly.

Regarding the dipolar charge, we consider the buildup of an asymmetric charge density at the microgel surface which results by slightly displacing two otherwise completely overlapped, oppositely charged spheres, carrying, respectively, uniform monopole charges $\pm\varrho_{uni}(\mathbf{r}) = \pm\rho_0 e\Theta(a - r)$ along the field direction $\hat{\mathbf{e}}_z$, as depicted in Figure 2b. Note that the fictitious monopole charge density $\rho_0 e$ has nothing to do with the real monopole charge distribution on the microgels, but it is simply an intermediate mathematical tool to produce the sought for dipolar charge distribution induced by the external electric field. Our approximation to the dipole contributions is then obtained by considering the formal limit in which this displacement $\mathbf{d} = d\hat{\mathbf{e}}_z$ vanishes, while keeping the product $\rho_0 ed \equiv P$ constant in magnitude:

$$\varrho_D(\mathbf{r}) = \lim_{\substack{d\to 0 \\ \rho_0\to\infty}} [\varrho_{uni}(\mathbf{r} + \mathbf{d}) - \varrho_{uni}(\mathbf{r})] = \lim_{\rho_0 ed\to P} \nabla\varrho_{uni}(\mathbf{r})\cdot\mathbf{d} \tag{2}$$

Replacing the uniform monopole charge of magnitude (per unit of e) ρ_0 homogeneously distributed over the spherical microgel, $\varrho_{uni}(\mathbf{r}) = \rho_0 e\Theta(a - r)$, in the above relation, we obtain

$$\varrho_D(\mathbf{r}) = e\rho_0\delta(r - a)\hat{\mathbf{e}}_r\cdot\mathbf{d} = P\delta(r - a)\cos\theta \tag{3}$$

where θ is the polar angle between the position vector $\mathbf{r}$ and the field direction. Evidently, we obtain a surface charge density modulated by the cosine of the angle with the z-axis. Moreover, we have defined the reduced polarization P (dipole moment per unit volume) as the limit in which the displacement d vanishes, and at the same time the monopole distribution $\rho_0 e$ goes to infinity, in such a way as to keep the product $P = \rho_0 ed$ constant. This construction of the dipolar charge distribution is consistent with the physical picture of a uniform dipole moment density $\mathbf{P}$ of point-like dipoles aligned toward the field direction, such that the internal charges exactly cancel each other, leaving only a nonvanishing charge density at the particle boundaries.

In practice, the frequency-dependent polarization $\mathbf{P}$ should be related to the ionic charge density $\varrho_{ind}(\mathbf{r})$ induced by the electric field inside the microgel *via*:

$$\mathbf{P} = \frac{3}{4\pi a^3}\int d\mathbf{r}\varrho_{ind}(\mathbf{r})z\hat{\mathbf{e}}_z \tag{4}$$

It is clear from this exact relation that the microgel polarization $\mathbf{P} = \rho_0 e\mathbf{d}$ we have defined to describe time-averaged field effects is an effective parameter, which, in taking quantitatively into account the complex charge diffusion within the polymer meshes, ultimately leads to dipolar microgel interactions. In a static situation, eq 4 yields a fixed polarization, whereas in our case the latter oscillates with time, following the external field. The cycled-averaged induced polarization of a single microgel is, of course, zero; however, the instantaneous induced dipole moments of any two microgels in the solution are always parallel to one another, and the time-independent dipole−dipole effective interaction to be derived in what follows should be understood as the average of the instantaneous one over one period of the field. This quantity scales with P^2, thus the polarization P above should be understood in the context of the experiment at hand as the root-mean-square (rms) of the microgels' instantaneous polarization. It follows that P is expected to be proportional to the value E_{rms} of the imposed field, with some frequency-dependent proportionality constant, which will be determined later on the basis of experimental results from dielectric spectroscopy.[73]

Due to the polar symmetry of the dipolar charge distribution, the electrostatic pair potential described by eq 1 will comprise only monopole−monopole and dipole−dipole interactions, the crossed dipole−monopole interactions vanishing identically. To see why this happens, let us consider the net force on particle 2 of Figure 2a resulting from its dipole−monopole coupling with the charges on particle 1. The total force exerted by the

DOI: 10.1021/acsnano.7b08843
ACS Nano 2018, 12, 4321−4337

monopole charge of particle 1 on the dipolar charge distribution of particle 2 will be completely counterbalanced by the force that the dipolar charge distribution of particle 1 exerts on the monopole of particle 2. This symmetry should breakdown in the case of polydisperse microgels, in which case the charge asymmetry between different components may give rise to nontrivial monopole−dipole couplings. We will disregard such polydispersity effects on what follows and focus solely on the monopole−monopole and dipole−dipole electrostatic interactions.

We consider an ionic solution of such microgels in monovalent salt with counter- and co-ion bulk concentrations ρ_b. Applying the linearized approximation of Poisson−Boltzmann theory, that is, the Debye−Hückel theory, one obtains the result that both the monopole and the dipole potentials $\psi_M(\mathbf{r})$ and $\psi_D(\mathbf{r})$ are screened at large distances $|\mathbf{r}| \gg a$ by the same factor $\sim \exp(-\kappa r)$, where $1/\kappa$ is the Debye screening length.[85] This arises out of the fact that the Debye−Hückel approximation is a linear theory, and therefore the monopole and dipole potentials separately obey, in the static case, the equations:

$$(\nabla^2 - \kappa^2)\psi_M(\mathbf{r}) = -\frac{4\pi}{\varepsilon}\varrho_M(\mathbf{r}) \tag{5a}$$

$$(\nabla^2 - \kappa^2)\psi_D(\mathbf{r}) = -\frac{4\pi}{\varepsilon}\varrho_D(\mathbf{r}) \tag{5b}$$

where $\varepsilon = 80$ is the water permittivity, $\kappa = \sqrt{4\pi\lambda_B(2\rho_b + Z\rho)}$ is the inverse Debye screening length, with ρ being the overall microgel concentration and $\lambda_B = \beta e^2/\varepsilon$ is the Bjerrum length, which measures the distance at which thermal and electrostatic energies have similar strengths, $\beta = (k_B T)^{-1}$ being the inverse temperature ($\lambda_B \cong 7.2$ Å in the present case of an aqueous solution at room temperature). Notice that the inverse Debye screening length—and therefore the monopole and dipole potentials—explicitly depends on the microgel concentration. This is because the above approach is equivalent to linearizing the potential around a Donnan potential which ensures overall charge neutrality, rendering the pair interactions density dependent. For the case of time-dependent external fields as the one at hand, we need to generalize this approach in a heuristic way, which will be afterward justified by comparison with experimental results. In particular, the screening of the dipolar interactions has to be reconsidered for a number of reasons, namely the following.

(1) The dipolar attractions along the field direction bring forward the formation of (short or long) chains. The modeling of each dipolar microgel as an idealized surface charge is appropriate for larger separations but not for close contacts. A more realistic scenario for close approaches, which is fully supported by experimental evidence[86] (also: S. Nöjd, C. Hirst, J. Schmitt, M. Obiols-Rabasa, A. Radulescu, P. S. Mohanty, and P. Schurtenberger, unpublished data), is that upon close approach or chain formation two neighboring microgels interpenetrate, so that the oppositely charged regions on the two fully overlap. The physical situation thus is much more akin to two superimposed patches of opposite charge without any intervening electrolyte, implying a strong *unscreened* attraction between the two.

(2) The linear screening assumption is also questionable from a formal point of view for overlapping, chain-forming microgels, since it is based on the assumption of weak attractions, of order of the thermal energy. Stable chain formation as in the present case, on the other hand, requires stronger attractions along the field direction.

(3) Finally, it should be kept in mind that the dipolar interaction introduced here is a notion based on time averages, and thus the screening length of the dipoles is expected to have a frequency dependence. Indeed, as $f \to 0$, full screening is expected, whereas at very high frequencies, whose inverse is smaller than the characteristic relaxation time of a microgel, two microgel particles in a chain have no time to detach during the part of the cycle in which the external field is close to zero, and thus no screening of the patch attractions should take place in that case. At intermediate frequencies, we expect the near-field attractions to be screened for a part of a cycle and unscreened for the rest.

Guided by the above considerations, we make a generalization of the static Debye−Hückel approach by introducing two different screening lengths for the monopoles and the dipoles, namely we replace eqs 5a and 5b with

$$(\nabla^2 - \kappa_M^2)\psi_M(\mathbf{r}) = -\frac{4\pi}{\varepsilon}\varrho_M(\mathbf{r}) \tag{6a}$$

$$(\nabla^2 - \kappa_D^2)\psi_D(\mathbf{r}) = -\frac{4\pi}{\varepsilon}\varrho_D(\mathbf{r}) \tag{6b}$$

which introduce two different inverse screening lengths, κ_M for the monopoles and κ_D for the dipoles. As the former are static, $\kappa_M = \kappa$, but, in general, the dipoles will be more weakly screened and thus $\kappa_D \leq \kappa_M$. This means that ions will screen more intensively the monopole interactions, as they are able to react to these equilibrium interactions within very large time scales, in comparison with the dipole interactions. On the physical grounds explained above, we postulate that $\kappa_D \to \kappa_M$ as $f \to 0$ and $\kappa_D \to 0$ as $f \to \infty$. The formal solutions to eqs 6a and 6b can be readily written in terms of the corresponding Green function for vanishing boundary conditions in the open system $G(\mathbf{r}, \mathbf{r}') = -e^{-\kappa|\mathbf{r}-\mathbf{r}'|}/(4\pi|\mathbf{r} - \mathbf{r}'|)$ as

$$\psi_{M,D}(\mathbf{r}) = \frac{1}{\varepsilon}\int \varrho_{M,D}(\mathbf{r}')\frac{e^{-\kappa_{M,D}|\mathbf{r}-\mathbf{r}'|}}{|\mathbf{r} - \mathbf{r}'|}d\mathbf{r}' \tag{7}$$

The above integrals can be solved analytically for both distributions $\varrho_M(\mathbf{r})$ and $\varrho_D(\mathbf{r})$ to provide explicit closed expressions for the effective electrostatic monopole and dipole interactions. Following eq 1, the resulting monopole−monopole $u_{MM}(\mathbf{r})$ and dipole−dipole $u_{DD}(\mathbf{r})$ interactions at the linear regime under consideration can thus be written as

$$u_{MM}(\mathbf{r}) = \int \varrho_M(\mathbf{r}')\psi_M(\mathbf{r}' - \mathbf{r})d\mathbf{r}' \tag{8}$$

$$u_{DD}(\mathbf{r}) = \int \varrho_D(\mathbf{r}')\psi_D(\mathbf{r}' - \mathbf{r})d\mathbf{r}' \tag{9}$$

We are now going to work out these monopole−monopole and dipole−dipole contributions to the total electrostatic pair potential separately.

Monopole−Monopole Interactions. Substitution of the uniform monopole charge $\varrho_M(r) = 3Ze\Theta(a - r)/(4\pi a^3)$ in eq 7 results in the following monopole electrostatic potential:

$$\psi_M(r) = \frac{3Ze}{\kappa_M^3 a^3 \varepsilon}F(\kappa_M a)\frac{e^{-\kappa_M r}}{r}, \ (r \geq a) \tag{10}$$

DOI: 10.1021/acsnano.7b08843
ACS Nano 2018, 12, 4321−4337

$$\psi_M(r) = \frac{3Ze}{\kappa_M^3 a^3 \varepsilon r}[\kappa_M r - e^{-\kappa_M a}(\kappa_M a + 1)\sinh(\kappa_M r)],\ (r < a) \tag{11}$$

where we have defined the function $F(x) \equiv x\cosh(x) - \sinh(x)$. The monopole−monopole pair interactions can be now obtained by replacing the above potentials in eq 8, together with the monopole charge $\rho_M(r)$. The resulting monopole−monopole pair potential at regions beyond particle overlap distances $(r \geq 2a)$ is

$$\beta u_{MM}(r) = \lambda_B \left(\frac{3ZF(\kappa_M a)}{\kappa_M^3 a^3}\right)^2 \frac{e^{-\kappa_M r}}{r},\ (r \geq 2a) \tag{12}$$

The above pair interaction is the usual screened Yukawa potential with an effective charge which accounts for finite microgel size as well as for the ionic adsorption into their soft cores. At distances shorter than particle overlap, the monopole pair potential reads as

$$\beta u_{MM}(r) = \frac{9Z^2\lambda_B}{2\kappa_M^6 a^6 r}[\gamma(r) - e^{-\kappa_M a}(\kappa_M a + 1)[\kappa_M a\sinh(\kappa_M(r-a)) + \cosh(\kappa_M(r-a)) - e^{-\kappa_M r}F(\kappa_M a)]],\ (r < 2a) \tag{13}$$

where the function $\gamma(r)$ reads as

$$\gamma(r) = \kappa_M^4\left[\left(\frac{r^2 - a^2}{4}\right)(r^2 - 2ra) + \frac{r}{3}(a^3 - (r-a)^3) - \frac{a^4 - (r-a)^4}{8}\right] + \frac{\kappa_M^2}{2}(r^2 - 2a^2) + 1 \tag{14}$$

Not surprisingly, the above expressions for the effective monopole pair potentials are identical to those obtained in early contributions for microgels in the absence of external fields.[87,88] This is due to the complete decoupling of monopole and dipole interactions at this linear level of approximation.

Dipole−Dipole Interactions. Despite the calculations being a bit more involved, the dipole−dipole pair interactions can also be analytically obtained following essentially the same steps outlined above for the monopole interactions. Upon substitution of the microgel dipolar charge distribution $\varrho_D(\mathbf{r}') = P\delta(r' - a)\cos\theta'$ in eq 7 for the dipole mean potential, we obtain the following dipole electrostatic potential outside the microgel volume $(r \geq a)$:

$$\psi_D(\mathbf{r}) = \frac{4\pi P}{\varepsilon\kappa_D^3}F(\kappa_D a)\frac{e^{-\kappa_D r}}{r^2}(\kappa_D r + 1)\cos\theta,\ (r \geq a) \tag{15}$$

whereas the dipole potential inside the microgel $(r < a)$ reads as

$$\psi_D(\mathbf{r}) = \frac{4\pi P}{\varepsilon\kappa_D^3 r^2}e^{-\kappa_D a}(\kappa_D a + 1)F(\kappa_D r)\cos\theta,\ (r < a) \tag{16}$$

The effective dipole interactions can now be obtained by replacing the dipole potentials in eq 9, together with the dipole charge distribution $\varrho_D(\mathbf{r}') = P\delta(r'-a)\cos\theta'$. After some algebraic manipulations, the details of which we will omit here, we arrive at effective pair interactions in the form:

$$\beta u_{DD}(\mathbf{r}) = \beta u_{DD}^{(0)}(r) + \beta u_{DD}^{(2)}(r)P_2(\cos\theta) \tag{17}$$

where now $\cos\theta = \hat{\mathbf{e}}_r \cdot \hat{\mathbf{e}}_z$ is the angle between the vector $\mathbf{r}$ connecting the center of the two microgels and the z-axis, and $P_2(x) = (3x^2-1)/2$ is the usual second-order Legendre polynomial. For distances beyond particle overlaps $(r \geq 2a)$, the radial coefficients $\beta u_{DD}^{(0)}(r)$ and $\beta u_{DD}^{(2)}(r)$ are

$$\beta u_{DD}^{(0)}(r) = -\left(\frac{3\tau F(\kappa_D a)}{\kappa_D^2 a^2}\right)^2 \frac{\lambda_B}{3}\frac{e^{-\kappa_D r}}{r} \tag{18a}$$

$$\beta u_{DD}^{(2)}(r) = -\left(\frac{3\tau F(\kappa_D a)}{\kappa_D^2 a^2}\right)^2 \frac{2\lambda_B}{3}\frac{e^{-\kappa_D r}}{\kappa_D^2 r^3}(\kappa_D r + 1)\left(3 + \frac{\kappa_D^2 r^2}{(\kappa_D r + 1)}\right) \tag{18b}$$

Here, we have defined the dimensionless parameter $\tau \equiv 4\pi a^2 P/(3e) = p/(ae)$, where $p = 4\pi a^3 P/3$ is the (rms strength of the) microgel dipole moment. The coefficient τ is the effective, dimensionless parameter, which expresses the strength of the field-induced dipole interactions. It implicitly depends on both strength and frequency of the driving applied field and should contain the average information on how the charges inside the microgel are spatially separated as a response to the field. By construction, it should also comprise nonlinear effects from the ionic distributions at the double-layer as well as possible many-body effects. This is because this quantity is defined within a linear response approach, which leads to pairwise effective interactions. Extension of these interactions to more general situations requires thus the incorporation of nonlinear and many-body effects into this effective parameter. This is quite similar to what is usually done in the case of colloidal interactions, whereby the traditional Derjaguin−Landau−Verwey−Overbeek (DLVO) pair interactions are generalized to circumstances of nonlinear screening (ionic condensation) and many-body effects (overlapping of electric double layers) provided these effects are properly incorporated into an effective, renormalized colloidal charge.[34,47]

At regions of particle superposition $(r < 2a)$, the radial coefficients $\beta u_{DD}^{(0)}(r)$ and $\beta u_{DD}^{(2)}(r)$ take the form:

$$\beta u_{DD}^{(0)}(r) = -\left(\frac{3\tau}{\kappa_D a}\right)^2 \frac{\lambda_B}{6a}\frac{e^{-\kappa_D a}}{\kappa_D r}\left\{(\kappa_D a + 1)\left[\left(\frac{r^2}{2a^2} - 1\right)\sinh(\kappa_D a) - \sinh(\kappa_D(r-a)) + \frac{1}{\kappa_D a}[\cosh(\kappa_D a) - \cosh(\kappa_D(r-a))]\right] + \kappa_D a F(\kappa_D a)\left[\frac{r^2}{2a^2} - \frac{1}{\kappa_D a} - 1 + \left(1 + \frac{1}{\kappa_D a}\right)e^{-\kappa_D r}\right]\right\} \tag{19a}$$

$$\beta u_{DD}^{(2)}(r) = -\left(\frac{3\tau}{\kappa_D a}\right)^2 \frac{\lambda_B}{a}\frac{e^{-\kappa_D a}}{\kappa_D^2 r^2}\left\{(\kappa_D a + 1)\left[\left(\frac{r-a}{\kappa_D r a} - \frac{\kappa_D r}{3}\right)\sinh(\kappa_D(r-a)) + \left(1 - \frac{1}{\kappa_D^2 r a} - \frac{r}{3a}\right)\cosh(\kappa_D(r-a)) + \left(\frac{\kappa_D r}{6} + \frac{\kappa_D r^3}{24a^2} - \frac{1}{\kappa_D r}\right)\sinh(\kappa_D a) + \left(\frac{1}{\kappa_D^2 r a} - \frac{r}{6a}\right)\cosh(\kappa_D a)\right] + \frac{F(\kappa_D a)}{\kappa_D a}\left[\frac{\kappa_D r}{6} + \frac{\kappa_D^2 r^3}{24a} + \frac{\kappa_D^2 r a}{6} - \frac{\kappa_D a + 1}{\kappa_D r} + \left(\frac{\kappa_D^2 r a}{3} + \frac{\kappa_D r}{3} + \frac{\kappa_D(r+a) + 1}{\kappa_D r} + \kappa_D a\right)e^{-\kappa_D r}\right]\right\} \tag{19b}$$

Equations 17, 18a, 18b, 19a, and 19b completely specify the effective, field-induced dipole interactions all over the space. Apart from the microgel size, these interactions are fully determined by two dimensionless strength parameters: the coefficient τ which accounts for the induced dipole moment inside the polymer backbones and the parameter $\kappa_D a$ which is

DOI: 10.1021/acsnano.7b08843
ACS Nano 2018, 12, 4321−4337

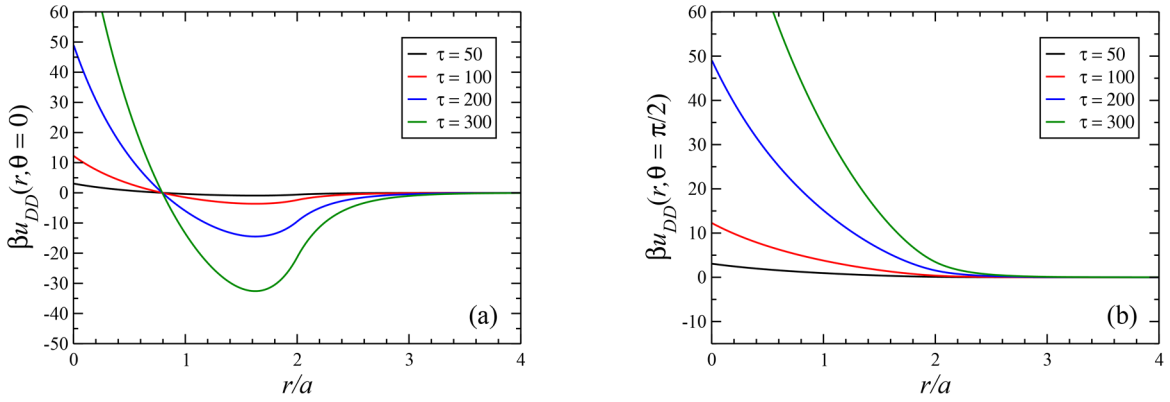

Figure 3. Typical dipole−dipole effective potentials corresponding to different dimensionless dipole moments $\tau = p/(ae)$ and at the directions parallel (a) and orthogonal (b) to the applied field. Here we chose a microgel radius a = 0.3 μm and an inverse dipole screening length κ_D = 8.34 μm^{-1}.

related to the anisotropic rearrangement of ions in response to the applied field, effectively leading to screened dipole−dipole interactions. While the latter depends only on the driving frequency f of the external field, the former should implicitly depend on both strength and frequency of the applied AC field.

In Figure 3 we show some typical features of the effective dipole−dipole pair potential across both parallel (Figure 3a) and perpendicular (Figure 3b) field directions. While these interactions are purely repulsive along the planes perpendicular to the applied field, they become attractive at larger distances in the direction parallel to the field. As the dipole moment, described by the dimensionless parameter τ, grows larger, a potential well starts emerging along the field direction. The dipole interactions across intermediate directions interpolate between these different types of behavior. For the largest dipole moment τ = 300, the depth of this potential well is about 40 times the thermal energy, anticipating a strong tendency to chain-like formations across the field direction at higher dipole moments, in accordance to the experimental observations described previously. However, it is important to notice that this potential well lies at distances sufficiently shorter than particle−particle contact, whereby both monopole−monopole and elastic repulsion (as we shall see in the next section) become very strong. It is the specific interplay between these competing contributions that will dictate the self-assembly properties of these systems.

Although the expressions for the effective dipolar interactions are rather cumbersome and difficult to be assigned with transparent physical interpretations, it is important to notice that they will assume very simple forms in the limit of unscreened dipoles ($\kappa_D \to 0$). Considering this limiting behavior on the expressions above, the radial coefficients in regions where $r \geq 2a$ become

$$\beta u_{DD}^{(0)} = 0, \ (r \geq 2a) \tag{20a}$$

$$\beta u_{DD}^{(2)} = -\frac{2\lambda_B a^2 \tau^2}{r^3} (r \geq 2a) \tag{20b}$$

whereas for overlapping particles, they read as

$$\beta u_{DD}^{(0)} = \frac{3\lambda_B \tau^2}{2a}\left(\frac{r^3}{24a^3} - \frac{r}{2a} + \frac{2}{3}\right), \ (r < 2a) \tag{21a}$$

$$\beta u_{DD}^{(2)} = \frac{3\lambda_B \tau^2}{8a}\left(\frac{r^3}{6a^3} - \frac{r}{a}\right), \ (r < 2a) \tag{21b}$$

Interesting enough, the zero-order contribution in the dipole expansion is nonvanishing even in the case of unscreened overlapping microgels. This finite size contribution obviously disappears in the limit of point-like dipoles $a \to 0$, whereby the usual dipole interactions between a pair of aligned point dipoles $u_{DD}(\mathbf{r}) = (-2p^2/r^3)P_2(\cos\theta)$ is recovered.

Effective Pair Interactions. We are now in position to combine the electrostatic interactions obtained above and write down the total pair microgel potential. Apart from these electrostatic interactions, the microgels also experience a soft steric repulsion at contact, that is, for distances shorter than the particle diameter. We model this short-ranged soft repulsion through the well-known Hertz potential, which was previously found to quantitatively reproduce the structural correlations between microgels of similar cross-link density throughout the fluid region of the phase diagram.[89] It is however important to point out that this choice is completely phenomenological, as the Hertzian soft repulsion has been derived for the case of elastic and nonpenetrable spheres, while the particles here are able to interpenetrate.[86] Since this contribution is fully decoupled from the electrostatic ones, it simply adds up to the overlapping electrostatic pair potentials. The (dimensionless) Hertzian potential $\beta u_H(r)$ is given by[58]

$$\beta u_H(r) = \epsilon_H\left(1 - \frac{r}{2a}\right)^{5/2}\Theta(2a - r) \tag{22}$$

where ϵ_H is a dimensionless parameter that dictates the strength of the elastic repulsion at close contact. In practice, this quantity is related to the size and internal structure of microgels *via* $\epsilon_H = 8\ a^3/5Dk_BT$, where $D = (1 - \nu^2)/2K(1 - 2\nu)$, with ν being the Poisson's ratio and K the bulk modulus characteristic of the microgel material.[58,59]

The total anisotropic pair potential can be finally written as a combination of zero- and second-order contributions in a Legendre polynomials expansion as $\beta u_{\text{eff}}(\mathbf{r}) = \beta u_0(r) + \beta u_2(r) P_2(\cos\theta)$, where higher order multipole contributions vanish identically at this linear level of approximation. The coefficients $\beta u_0(r)$ and $\beta u_2(r)$ are written in terms of the contributions described above as

$$\beta u_0(r) = \beta u_H(r) + \beta u_{MM}(r) + \beta u_{DD}^{(0)}(r) \tag{23a}$$

DOI: 10.1021/acsnano.7b08843
ACS Nano 2018, 12, 4321−4337

$$\beta u_2(r) = \beta u_{DD}^{(2)}(r) \tag{23b}$$

The contributions from $\beta u_0(r)$ are given by eqs 12, 13, 18a, 19a, and 22, whereas the contributions in $\beta u_2(r)$ are fully specified in eqs 18b and 19b. Overall, the total pair interactions are fully determined by six independent coarse-graining parameters: λ_B/a (measuring the interplay between thermal and electrostatic energies at particle contact), the microgel bare charge Ze, the monopole inverse Debye screening length κ_M (controlling the screening of monopoles), the dipole inverse Debye screening length κ_D (which dictates the degree of dipole screening as a reaction to the field), the dimensionless microgel dipole moment $\tau = p/(ae)$, and the strength parameter of the Hertzian potential ϵ_H. A rich variety of effective interactions can be obtained upon changing these parameters. While monopole and elastic contributions are always repulsive, the dipole interactions continuously change between fully repulsive along the plane orthogonal to the field ($\theta = \pi/2$) to partially attractive along the field direction, where a potential well emerges at distances close to particle overlap (see Figure 3). We then expect that the degree of particle penetration along the field direction will be mostly dictated by the competition between dipole attraction, the monopole repulsion, and the short-ranged elastic interactions. We emphasize, however, that none of these quantities has been employed here as a fitting parameter; rather, we have extracted them from experimental data, and we have thereby performed a comparison of the ensuing theoretical pair correlations in the system with those measured in experiments. We are now going to analyze the structural features of this model system in light of experimental observations.

Comparison with Experiments. In order to test the accuracy of the proposed theoretical approach, we now proceed to compare its predictions for the structural properties against experimental results for the system described above. The first step toward this direction is to determine what the equilibrium (no field) effective parameters characteristic of this system are. Although the experiments were performed in the absence of added salt, the aqueous solution is in equilibrium with atmospheric carbon dioxide, which leads to the dissociation of a 1:1 electrolyte. The corresponding ionic strength has been obtained in a previous work (see ref 73) to be $I = 2.54 \times 10^{-6}$ M, resulting in an inverse Debye screening length $\kappa_b = 5.3$ μm^{-1}. Linearization of the far-field around a Donnan potential, which ensures overall charge neutrality, implies a density-dependent monopole inverse screening length $\kappa_M = \kappa_b\sqrt{1 + \kappa_{mon}^2/\kappa_b^2}$, where $\kappa_{mon}^2 = 4\pi\lambda_B Z\rho$ represents the screening contribution originated from dissociated counterions at the monomer backbones. Since both the overall packing fraction and particle size are directly accessible to measurements (from each the values $a = 0.53$ μm for the particle radii and $\phi_{eff} = 0.1$ for the overall packing fractions have been obtained, see subsection on experimental results), all we need to fully specify the equilibrium, zero-field properties are the particle charge Z and the strength of the Hertzian potential ϵ_H. To this end, we match the measured equilibrium pair correlation function in the absence of applied field with predictions for our model potential (setting $\tau = 0$), in the framework of integral equations in the hypernetted-chain (HNC) approximation, which is known to be quite accurate in predicting the structures of Yukawa-like systems.[58,90] The result of this approach is shown in Figure 4. A very good match between experimental and theoretical pair correlations is observed when the dimensionless coarse-graining parameters assume the values $Z = 100$ and $\epsilon_H = 800$, fixing the values of these quantities, as can be verified by Figure 4. Note that the resulting low microgel charge is in good agreement with independently determined experimental values of similar microgels.[73]

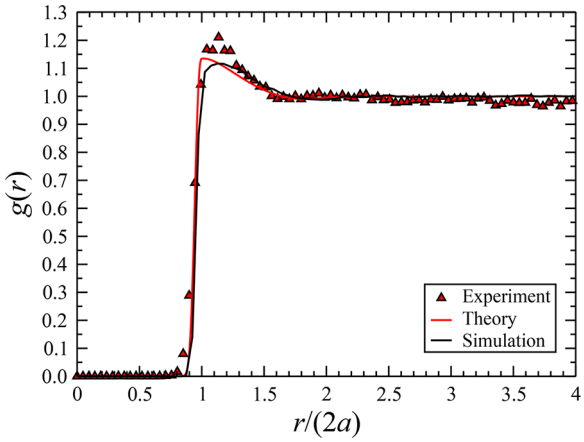

Figure 4. Radial distribution function in the absence of applied field. The microgel radius, as obtained from Dynamic light scattering is $a = 0.53$ μm, and the overall microgel volume fraction is $\phi_{eff} = 0.1$. The inverse monopole screening length is given by $\kappa_M = \kappa_b\sqrt{1 + \kappa_{mon}^2/\kappa_b^2}$, where $\kappa_{mon}^2 = 4\pi\lambda_B Z\rho$ represents the monomer screening contributions and $\kappa_b = 5.3$ μm^{-1} results from direct measurements of the amount of dissociated 1:1 electrolyte. The theoretical predictions from our coarse-graining model are obtained in the framework of the HNC integral equations approach (solid red line) and shows excellent agreement with experimental results (symbols) for the dimensionless effective parameters $Z = 100$, and $\epsilon_H = 800$. For the sake of completeness, the radial distribution function from MD simulations for the same system parameters (and $\tau = 0$) is also displayed (black solid curve).

The total effective potential corresponding to this set of parameters is shown in Figure 5 for different effective dipole moments τ in the unscreened limit ($\kappa_D = 0$), both along (left panel) and perpendicular (right panel) to the field direction. As the dipole moment becomes larger, the pair interactions become more repulsive at the perpendicular plane, and at the same time a potential well at close contact starts to emerge, again indicating the possibility of fluid-string transition. We have made here the assumption that the microgel radius a remains constant despite the accumulation of microgels along chains that form as the field strength increases, an approximation fully justified by the findings of recent, zero-average contrast experiments even at densities exceeding the overlap concentration.[86] Here it is important to point out that the zero average contrast method is the only direct experimental method which can be used to obtain information about the single particle size and shape at concentrations approaching or exceeding close packing. Although there are a number of experimental papers where deswelling of microgels has been reported,[37,60,91,92] the size determination is done indirectly either by fitting the structure factor described by an effective hard sphere model, using osmotic pressure measurements, or based on an estimate of the average interparticle distance, obtained using static light scattering (see ref 86 for a detailed discussion). Moreover, as can be seen in Figure 5a, the minimum of the total interaction potential for microgels aligned

DOI: 10.1021/acsnano.7b08843
ACS Nano 2018, 12, 4321−4337

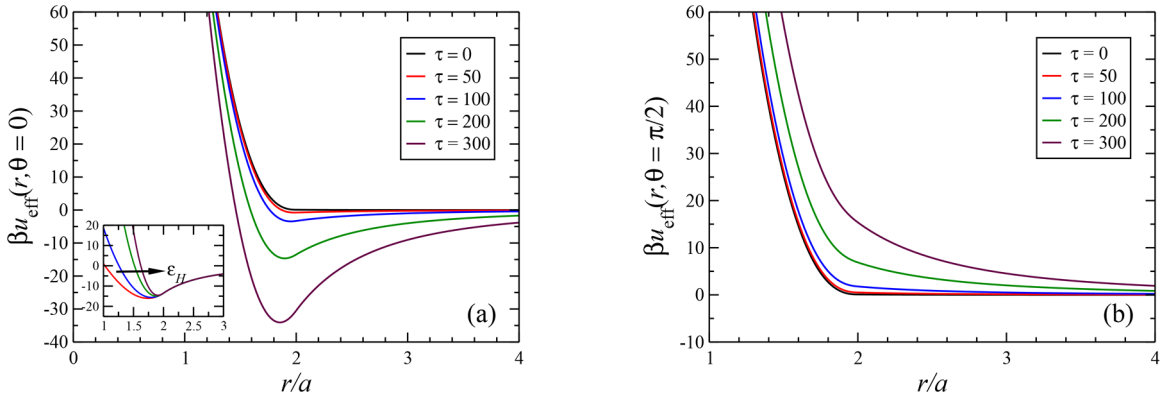

Figure 5. Effective pair potential corresponding to the monopole parameters obtained from the HNC fitting, for different values of the dimensionless dipole moments τ. The particle radius is a = 0.53 μm, its total monopole charge is Z = 100, the inverse monopole dipole screening length is κ_M = 5.26 μm^{-1}, and the strength parameter for the Hertz interaction is ϵ_H = 800. All the dipole interactions are unscreened, corresponding to κ_D = 0. In (a), the interactions are along the field direction, while in (b) they are perpendicular to the applied field. The inset in (a) shows the effects of changing the particle softness (as measured from the Hertz strength ϵ_H) on the effective pair interactions corresponding to τ = 200. The Hertzian strengths are in this case ϵ_H = 50, 100, 500, and 1000. The arrow indicates the direction of increasing ϵ_H.

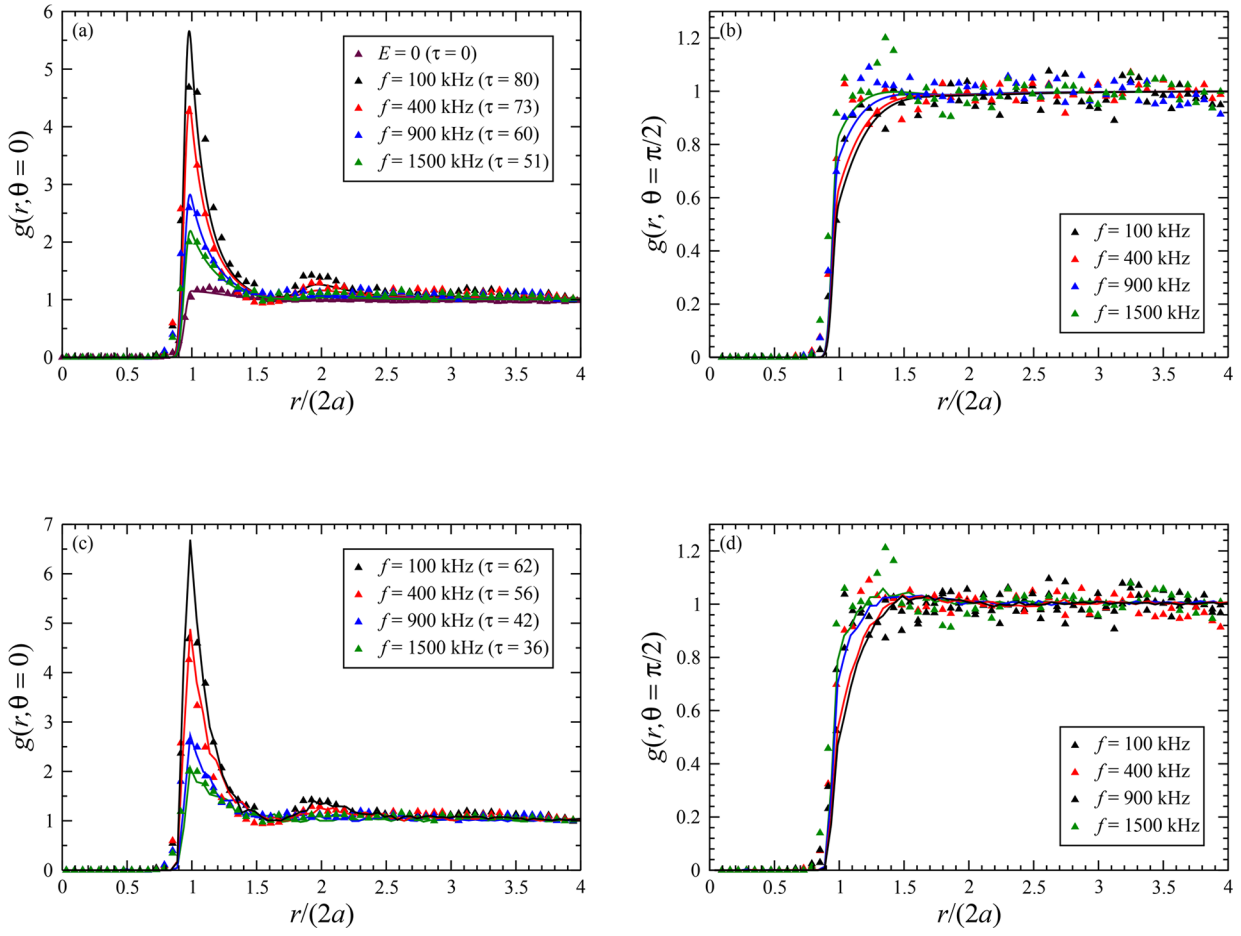

Figure 6. Pair correlation functions in directions parallel (a and c) and perpendicular (b and d) to the applied field for an AC field of strength E_{rms} = 0.0136 Vμm^{-1}. Symbols are experimental results, whereas solid lines are predictions from the HNC approach (a and b) and simulation results (c and d). In panel (a) we also show the result for the (isotropic) $g(r)$ for vanishing external field, E = 0, for completeness. The driving frequencies and the resulting dipole moments are indicated in the legends.

along the z-axis occurs at separations slightly smaller than the diameter $2a$, which is again fully consistent with experimental findings pointing toward microgel interpenetration rather than deformation along the direction of the field-induced chains (S. Nöjd, C. Hirst, J. Schmitt, M. Obiols-Rabasa, A. Radulescu, P. S. Mohanty, and P. Schurtenberger, unpublished data). This behavior is to be contrasted with the case of hard nanoparticles, which are not allowed to change their size or shape under

DOI: 10.1021/acsnano.7b08843
ACS Nano 2018, 12, 4321−4337

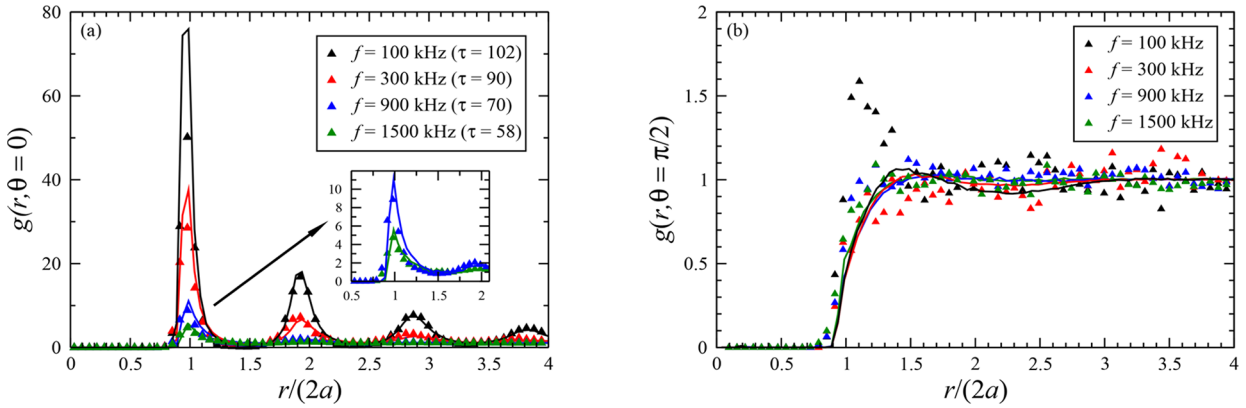

Figure 7. Pair correlation functions in both parallel (a) and perpendicular (b) directions to the field for an AC field of magnitude E_{rms} = 0.0227 Vμm^{-1}. Symbols are experimental results, whereas solid lines are simulation predictions. The driving frequencies and the resulting dipole moments are shown in the legends. The inset in panel (a) is a zoom-in at the main peaks of the two higher frequencies, which are obscured due to the chosen scale.

compression. Since soft nanoparticles are able to overlap each other in the presence of attractive interactions, these particles can be strongly attached to one another to form close-packed configurations (T. Colla, R. Blaak, and C. N. Likos, unpublihsed data). This will clearly favor the formation of chain-like structures across a direction where the interactions are strongly attractive. Such tendency of particles to come very close together in such a way as to minimize their mutual interacting energy is manifested by the presence of a potential well in their pair interactions. In the inset of Figure 5a, we show the effects of particle stiffness on their effective pair potentials. We can see that the stiffness of the short-ranged repulsion decreases the depth of the potential well, which is further shifted to longer interparticle distances. This clearly indicates that soft particles tend to be more closely attached to each other across the field direction, a mechanism that should definitely favor the string formation along this direction.

To obtain the effective, frequency- and field-strength-dependent microgel dipole moments, we will make the assumption that frequencies in the range under investigation (100 kHz $\leq f \leq$ 1500 kHz) are too fast for the microgels that associate into chains to react, such that the counterions do not screen the near-overlap dipole interactions. This assumption is far from trivial and depends on the specific conditions underlying the system at hand. Indeed, a detailed description of the interplay between particle diffusion and attraction in the presence of driving fields is a rather challenging question.[93] In the present case, it is justified by recent theoretical and experimental dielectric spectroscopy investigations.[73] Our strategy here is to first obtain the frequency-dependent dipole moments in the absence of screening and then to test the validity of these hypothesis afterward, by comparing the results with available dielectric spectroscopy predictions. The comparisons with experimental data are performed for two different field strengths: E_{rms} = 0.0136 Vμm^{-1} and E_{rms} = 0.0227 Vμm^{-1}. We recall that the field strength and the induced dipole moment are proportional to each other, $p = \alpha(f)E_{rms}$, the frequency-dependent proportionality constant being the microgel polarizability $\alpha(f)$ in solution. We therefore expect that the ratio between dipole moments obtained at the same frequencies should coincide with the field strength ratio, $\tau_1/\tau_2 = E_1/E_2$. The dipole moments $\tau(f)$ are computed by fitting the measured data *via* the anisotropic hypernetted chain (HNC) integral equation approximation and MD simulations. The former has the advantage of being computationally much more efficient, providing a simple way of estimating the values of the effective dipole moment τ. Its predictions are however significantly less reliable than the simulation ones, as the HNC approach is known to underestimate the pair correlations in the case of unscreened Coulombic interactions. Furthermore, the approximation fails to provide convergent solutions close to the onset of structural transitions.

In Figure 6 we show comparisons between theory (solid lines) and experiments (symbols) at the directions parallel (left panels) and perpendicular (right panels) to the field at the field strength E_{rms} = 0.0136 Vμm^{-1}. A very good agreement is found for both HNC (upper panels) and simulation (lower panels) approaches. The predicted frequency-dependent dipole moments τ are however different in the two approaches. This discrepancy can be assigned to the inaccuracy of the HNC approach in capturing the structure of unscreened dipole interactions, which are known to be underestimated in this approach. Although the magnitudes are slightly different, both approaches predict similar behaviors for the induced dipole moment, which decreases at similar rates as the driving frequency increases.

To further test the predictive power of the proposed theory, we compare simulation results with experimental data for the case of a larger field strength, E_{rms} = 0.0227 Vμm^{-1}. For such larger field magnitude, the HNC approach starts to breakdown at smaller frequencies, indicating the emergence of strong structural ordering in this regime. The results for the in and out of plane correlation functions from both experiments (symbols) and simulations (solid lines) are displayed in Figure 7. Here we see that the overall agreement between theory and experiment is again very good, except for the correlation function perpendicular to the field direction at frequency f = 100 kHz (see Figure 7b). This disagreement most likely indicates that the experimental point at E_{rms} = 0.0227 Vμm^{-1} (frequency f = 100 kHz) is already in the coexistence region, where a locally ordered phase coexists with a string-fluid.[64] Chain−chain aggregation is clearly visible in the 2D CLSM image (Figure 9). Usually a phase transition close to freezing is governed by kinetics, which in turn depends here on the aggregation of chains into dense structures. These structures ultimately evolve into a stable ordered phase.[94] However, our present work primarily focuses on comparing the experimentally obtained structural correlation functions in the equilibrium fluid phase,

DOI: 10.1021/acsnano.7b08843
ACS Nano 2018, 12, 4321−4337

covering the isotropic fluid to the fluid-string phase. Although the theoretical predictions for the perpendicular field structure do show a slight increase in particle ordering at f = 100 kHz, it is still far off the experimental data. This might be an indication that the emergence of chain ordering is shifted to higher effective dipole moments. A detailed combined theoretical/experimental analysis of the rich phase diagram goes beyond the scope of this work and will be the subject of a future investigation.

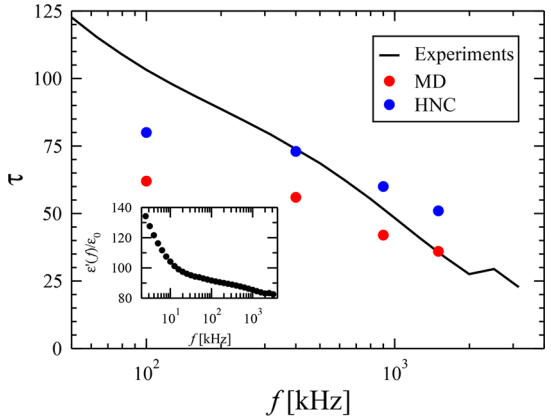

Figure 8. Dimensionless dipole moments $\tau(f)$ for an external electric field with strength E_{rms} = 0.0136 Vμm^{-1}, depending on the frequency f of the latter. Results obtained from dielectric spectroscopy measurements using eq 26 are shown as the solid line, together with those obtained from the theoretical approach in the context of the HNC approximation (blue dots) and MD simulations (red dots). The inset shows the dielectric spectroscopy data from which the dipole moments of the main plot have been extracted, following eq 26.

It is important to note that the ratio between the two electric fields under consideration, $E_2/E_1 \cong 1.67$, matches within a few percent with the ratios between the dipole moments corresponding to the same driving frequency, confirming the robustness of the proposed theoretical approach. This trend is also verified for the smallest driving frequency f = 100 kHz, which strongly suggests that our initial assumption, namely the nearly absence of screening for the dipole interactions at this frequency domain, is indeed appropriate. The theoretical results for the dipole moments for the two different samples under investigation are summarized in Table 1. A direct comparison between experimental CLSM images and simulation snapshots is shown in Figure 9, underlying visually the excellent agreement between the two.

As a final test for the accuracy of our theoretical approach, we now compare the obtained dipole moments with results from dielectric spectroscopy measurements[73] that allow us to extract the frequency-dependent permittivity at an applied field strength of E_{rms} = 0.0136 Vμm^{-1}. In such measurements, the

Table 1. Dimensionless Dipole Moments $\tau = p/(ea)$ Obtained from Integral Equations in the HNC Approximation and MD Simulations

	E_{rms} = 0.0136 Vμm^{-1}				E_{rms} = 0.0227 Vμm^{-1}			
f [kHz]	100	400	900	1500	100	300	900	1500
τ (MD)	62	56	42	36	102	90	70	58
τ (HNC)	80	73	60	51	–	–	95	77

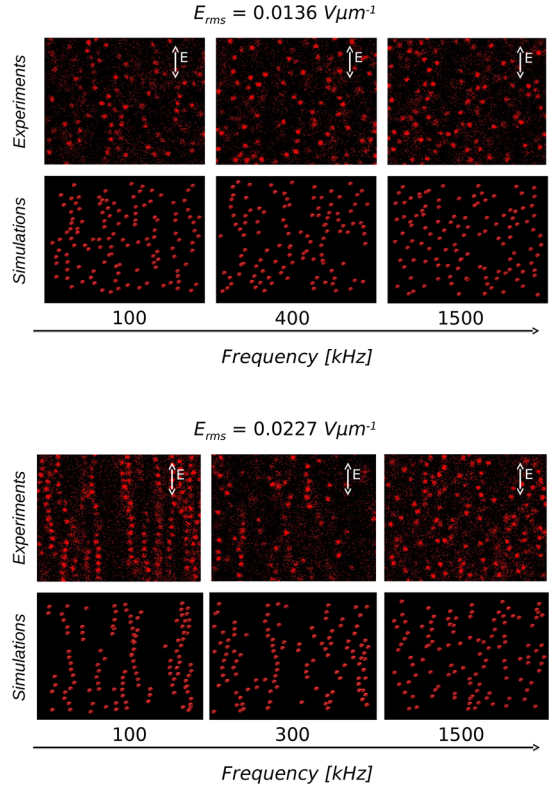

Figure 9. CLSM images (upper rows) and simulation snapshots (lower rows) of the microgel system at frequencies and electric field strengths as indicated on the axes.

overall real part of the system's relative permittivity $\varepsilon'(f)/\varepsilon_0$ (where ε_0 is the vacuum permittivity) can be obtained as a function of the imposed frequency. Experimentally, the complex dielectric permittivity of deionized ionic PNIPAM microgel suspensions at different concentrations over a wide frequency range from 10 Hz to 10^7 Hz in the swollen state (at T = 20 °C) was measured. The particles used had an identical cross-link density and a comparable size of a_H = 578 nm (see ref 73 for details).

The experimentally determined quantity $\varepsilon'(f)$ connects the rms in-phase polarization of the whole material, $\mathcal{P}(f)$, with the applied electric field via:

$$\mathcal{P}(f) = (\varepsilon'(f) - \varepsilon_0)E_{rms} \quad (24)$$

We employed SI units in eq 24 to comply with notation used in ref 73, whereas Gauss units have been used in the theoretical part. There is no conflict, however, since the quantity $\tau(f)$ is dimensionless, and thus it attains the same value in all systems of units. Due care must be taken in converting this measured quantity into the effective dipole moment $\tau(f)$, which is the main input in our coarse-graining approach. Indeed, the dipole moment defined in our theoretical model is the one assigned to one individual microgel, which builds up as a response to the electric field. This quantity is conceived to be on top of any effects of the field on the (strongly polarizable) solvent environment the particles are embedded in. What we need as input in our coarse-graining approach is therefore the excess dipole moment obtained *over* the solvent contributions, properly normalized with the particle number of the solution; it is then necessary to remove the solvent contribution from the measured overall permittivity. Replacing in eq 24 the quantity

DOI: 10.1021/acsnano.7b08843
ACS Nano 2018, 12, 4321−4337

$\varepsilon'(f)$ with the dielectric constant of water, ε_w, we obtain the polarization $\mathcal{P}_w$ due to the solvent. The difference $\mathcal{P}(f) - \mathcal{P}_w$ is the excess polarization due to all N_m microgel particles in the volume V with number density $\rho = N_m/V = 3\phi_{\text{eff}}/(4\pi a^3)$. Since each microgel has been assumed to contribute an identical excess rms-dipole moment p, it follows:

$$\mathcal{P}(f) - \mathcal{P}_w = \rho p \tag{25}$$

We can now obtain direct estimates for the value of $\tau(f)$ using the experimentally determined values of the dielectric constant $\varepsilon'(f)$ from ref 73 and the considerations above, as

$$\tau(f) = \frac{1}{3\phi_{\text{eff}}}\left(\frac{\varepsilon'(f)}{\varepsilon_0} - \varepsilon\right)\frac{4\pi\varepsilon_0 a^2}{e}E_{\text{rms}} \tag{26}$$

where $\varepsilon \equiv \varepsilon_w/\varepsilon_0 \cong 80$ is the relative permittivity of water.

The comparison of the dimensionless dipole moments $\tau(f)$ obtained from our simulation and the HNC approach with those obtained from eq 26 in conjunction with dielectric spectroscopy[73] are shown in Figure 8. Once more, very good agreement between theory and experiments is observed, especially at higher driving frequencies. This result is consistent with the overall physical picture outlined in our model approach: As the driving frequency becomes smaller, partial screening of the dipolar interactions will take place as the contact regions of the two microgels along the field direction temporarily separate from one another during the intervals in which the field is going through zero. Since we are considering fully unscreened interactions over all the spectra under investigation, it is not so surprising that small deviations in the obtained dipole moments might appear for smaller frequencies. Indeed, a perfect match between the experimental and theoretical dipole moments at the smallest frequency f = 100 kHz and lower field strength E_{rms} = 0.0136 Vμm^{-1} can be obtained by assuming that the dipole screening length is about 90% of the monopole screening.

CONCLUSIONS

We have investigated the self-assembly properties of a system of ionic microgels driven by the influence of an external AC electric field. A rich variety of self-assembly structures have been experimentally observed in this system, ranging from string-fluid transitions along the field direction to ordered aggregates in the perpendicular direction. Even though it is well-known that induced dipole interactions might give rise to chain-like formations at sufficiently strong field strengths, a theoretical model capable of quantitatively describing these structural features in terms of quantities experimentally controlled is up to now still missing. By proposing a coarse-graining approach in which the most relevant field effects are accounted for *via* partially screened dipole interactions, we were able to reproduce the experimental data within a very good degree of accuracy, with the employment of a model system and effective parameters that incorporate complex physical aspects of the real system in a simple and intuitive fashion. It is important to notice that the observed good agreement between theory and experiments is restricted to fluid and fluid-string regions of the phase diagram. A systematic study covering different regions of the complex phase diagram[65] is a promising topic for future investigations.

The predictive power shown by the proposed approach can be potentially used to investigate this system under a variety of external conditions. In particular, the model can be applied to predict how the various self-assembly scenarios can be tuned by adjusting experimentally accessible quantities, therefore providing guidelines for future experimental investigations. Besides, the model can be used to shed light on the physical mechanisms responsible for the intriguing morphological transitions and dynamic behavior that can be triggered by controlling the applied field properties. This topic will be the subject of a future investigation.

METHODS

We now briefly specify some of the numerical as well as experimental techniques employed in this work. For further details on these topics, we refer the reader to more specific literature on both experimental[64,65] and numerical[95−101] methods.

Synthesis of Ionic Microgels and Zero-Field Characterization. Monodisperse ionic microgel particles having a cross-link density of 5 mol % are used as the experimental model system in the current study. The same ionic microgel particles were also used in our earlier work[64,65] for studying the density-dependent electric field-induced phase behavior at a frequency of 100 kHz. Briefly, these microgel particles were synthesized by free-radical precipitation polymerization using *N*-isopropylacrylamide (NIPAM) as the monomer, *N*,*N*-methylene-bis-acrylamide as a cross-linker, and acrylic acid was used as an ionic co-monomer. Methacryloxyethyl thiocarbamoyl rhodamine B (MRB) was covalently incorporated to fluorescently label the microgel particles. Details on the synthesis procedures can be found elsewhere.[64,65]

The particle size in the swollen state (at a temperature of 20 °C) was determined using static and dynamic light scattering (DLS) at a very dilute particle concentration using a modulated 3D cross-correlation DLS instrument (LS spectrometer, LS Instruments, Switzerland). From the measured intensity cross-correlation function, the hydrodynamic radius (a_H = 530 nm) was extracted using a first-order cumulant analysis.[64] A detailed description of the temperature-dependent swelling behavior was reported previously.[65]

Electric Field Experiments. Electric field experiments were carried out using fully deionized microgel suspensions at low density (ϕ_{eff} = 0.1) in the swollen state (T = 20 °C) in chemical equilibrium with atmospheric CO_2. Particle assembly was studied using an inverted confocal laser scanning microscope (CLSM) (Leica DMI6000 with a SP5 tandem scanner in the resonant mode of 50 frames/s) at 512 × 256 pixels, excitation wavelength of 543 nm, and using a 100× immersion objective with a numerical aperture of 1.4. With this microscope, we can get a resolution of 220 nm in x- and y-directions and of 600 nm in z-direction. Particles with a diameter σ = 20 pixel can be located with a subpixel accuracy of 11 nm in x- and y- and 23 nm in z-directions. The fast resonant scanner allows us to accurately track particles even at low concentrations in the fluid state. The samples were contained between two cover slides separated by a 120 μm spacer. One cover slip was coated with indium tin oxide (ITO) with a 1.56 ± 0.01 mm sample gap etched out, which ensures a homogeneous electric field in the sample area where CLSM experiments were performed. An AC electric field $\mathbf{E}(t)$ was applied in the image plane. The field experiments were carried out by varying the frequency in a range from 100 to 1500 kHz at three different, constant field strengths with magnitudes E_{rms} = 0.0136, 0.0227, and 0.0317 Vμm^{-1}. Observations were made at a sufficiently large distance from the cell wall to probe bulk suspension properties.

At low ϕ_{eff} = 0.1, particles are diffusive in nature. Due to the fact that CLSM has a poorer resolution along the z-direction and the resonant scanner is equipped to operate only along the x−y directions, we tracked particles in x−y plane only.[89] For a given value of electric field strength and frequency, we recorded 4000 to 5000 image frames from x−y scans in different positions of the bulk suspension in the plane containing the AC electric field. Image analysis was carried out using standard algorithms,[102] and the determined x- and y coordinates were subsequently used for the calculation of the radial distribution function along and perpendicular to the AC field direction. We represent the pair distribution function $g(\mathbf{r})$ in a spherical coordinate

DOI: 10.1021/acsnano.7b08843
ACS Nano 2018, 12, 4321−4337

system oriented along the field. Thus, $g(r,\theta)$ is a function of the radial distance r and the polar angle θ, with $\theta = 0$ along the field direction. We computed the pair distribution function *via* the local number density around a given particle. For each particle, the locations of all other particles were binned in terms of r (64 bins between 0 and r_{max} = 4.04 μm) and θ (11 bins between 0 and $\pi/2$). The result was averaged over particles and frames and normalized by the area associated with each bin. To avoid boundary effects, we did not include particles closer than r_{max} to any image edge in this average. The resulting two-dimensional (2D) number density distribution was divided by the overall (2D) number density as computed from the CLSM images. In the limit where the effective thickness of the imaged slice is small, our procedure gives the same $g(r,\theta)$ as would have been obtained from 3D data. The adequacy of this procedure had been already demonstrated in our earlier work[89] for the radial distribution function $g(r)$, which corresponds to the θ-average of $g(r,\theta)$. Hence, all experimental 2D $g(r)$ are compared with theoretical 3D $g(r)$.

Numerical Simulations. The simulation results have been obtained using *NVT* MD simulations for a system of N_m = 1000 microgels confined in a cubic box of size $L = (N_m/\rho)^{1/3}$, where ρ is the overall microgel density. Minimal image boundary conditions have been applied across all directions, with a cutoff distance of $r_c = 6a$ (or, equivalently, $r_c = 16.75\kappa_M^{-1}$) for the screened electrostatic interactions. The temperature was kept fixed using a Andersen thermostat. A total of $N_{step} = 4 \times 10^6$ time steps, long enough to suppress any considerable fluctuation on the pair correlations across any direction, has been considered. Averages were calculated by sampling configurations over intervals of 1000 time steps after an equilibration time of $N_e = 10^6$ time steps.

In order to be able to apply minimal image boundary conditions in the case of long-range dipole interactions, standard Ewald summation techniques have been applied for calculating dipolar forces in both real and reciprocal spaces.[103] To this end, a total of 729 **k**-vectors isotropically distributed have been considered, along with an Ewald parameter of $\alpha = 5/L$ for the real space, short-range Ewald interactions.

The Anisotropic HNC Approach. Apart from numerical simulation approach, the pair correlations for a given set of system parameters have been also obtained in the framework of the Ornstein−Zernike (OZ) equation. This equation assumes the following particularly simple form when written in the reciprocal Fourier space:

$$\hat{h}(\mathbf{k}) = \hat{c}(\mathbf{k}) + \rho\hat{h}(\mathbf{k})\hat{c}(\mathbf{k}) \tag{27}$$

where $\hat{h}(\mathbf{k})$ and $\hat{c}(\mathbf{k})$ are the Fourier components of the total and direct correlation functions, $h(\mathbf{r}) = g(\mathbf{r}) - 1$ and $c(\mathbf{r})$, respectively.

The symmetry of the effective pair potentials as expressed in terms of Legendre polynomials expansion strongly suggests that the pair correlations $g(\mathbf{r})$ can be expanded accordingly as

$$g(\mathbf{r}) = \sum_{l=0}^{l_M} g_l(r)P_l(\cos\theta) = \sum_{l=0}^{l_M} \sqrt{\frac{4\pi}{2l+1}}\, Y_l^0(\theta,\phi)g_l(r) \tag{28}$$

where θ and ϕ are the polar and azimuthal angles corresponding to the position vector **r**, and $Y_l^0(\theta,\phi)$ are spherical harmonics. The above sum is restricted to only even l values due to polar symmetry of the dipolar interactions, and l_M is the integer at which the series is numerically truncated.

In a similar fashion, the Fourier-transformed correlations are expressed in terms of such polar expansions as

$$\hat{h}(\mathbf{k}) = \sum_{l=0}^{l_M} \sqrt{\frac{4\pi}{2l+1}}\, Y_l^0(\theta',\phi')\hat{h}_l(k) \tag{29}$$

where now (θ',ϕ') represent polar and azimuthal angles corresponding to the reciprocal vector **k**. The coefficients $\hat{h}_l(k)$ are related to their real space counterparts $h_l(r)$ by means of a Henkel transformation of order l:

$$\hat{h}_l(k) = 4\pi i^l \int_0^\infty r^2 h_l(r) j_l(kr)\mathrm{d}r \tag{30}$$

with $j_l(kr)$ being spherical Bessel function of order l. In terms of the coefficients for the total correlations $\hat{h}_l(k)$ and the corresponding ones for the direct correlations $\hat{c}_l(k)$, the Ornstein−Zernike eq 27 can be simplified thanks to the orthogonality relation of spherical harmonics to

$$\hat{\Gamma}_{l_3}(k) = \rho \sum_{l_1 l_2} \hat{c}_{l_1}(k)(\hat{c}_{l_2}(k) + \hat{\Gamma}_{l_2}(k))C^2(l_1, l_2, l_3; 0, 0, 0) \tag{31}$$

where $\hat{\Gamma}(\mathbf{k}) \equiv \hat{h}(\mathbf{k}) - \hat{c}(\mathbf{k})$, ρ is the overall microgel concentration, and the symbols $C(l_1, l_2, l_3; m_1, m_2, m_3)$ represent usual Clebsch−Gordan coefficients.

In order to solve the above equations, further relations between the coefficients $\hat{\Gamma}_l(k)$ and $\hat{c}_l(k)$ are necessary. These are provided by the closure (approximate) relations to the OZ equations. Here we adopt the anisotropic version of the traditional hypernetted-chain (HNC) relation. It is well-known that this closure relation is quite reliable for the calculation of pair correlation functions in systems governed by Yukawa-like tails. Using the expansion for the pair correlations in real space, eq 28, the anisotropic version of the HNC equation can be written as

$$\sum_{l=0}^{l_M} \sqrt{\frac{4\pi}{2l+1}}\, Y_l^0(\theta,\phi)g_l(r) = \exp\left[\sum_{l_1=0}^{l_M} \sqrt{\frac{4\pi}{2l_1+1}}\, Y_{l_1}^0(\theta,\phi)(\Gamma_{l_1}(r) - \beta u_{l_1}(r))\right] \tag{32}$$

where $u_l(r)$ are the components of the pair interaction, given by eqs 23a and 23b. From a numerical point of view, the exponential term on the right-hand side of the above relation makes it difficult to get rid of the angular dependences and to express direct relations between the radial coefficients. One easy way to circumvent this problem is to use suitable upper ladder operators L_+, which raise the azimuthal m eigenvalues up by one unity. After some straightforward manipulations, we can directly relate the radial coefficients as

$$g_{l_3} = \sum_{l_1,l_2} \sqrt{\frac{l_1(l_1+1)}{l_3(l_3+1)}}\, C(l_1, l_2, l_3; 0, 0, 0)C(l_1, l_2, l_3; 0, 1, 1)g_{l_1}\alpha_{l_2} \tag{33}$$

for $l_1 \neq 0$ and $l_3 \neq 0$. Here we have defined the coefficients $\alpha_l(r) \equiv \Gamma_l(r) - \beta u_l(r)$. For numerical purposes, it is convenient to further rewrite the above relation in a matrix form $\mathbf{A}\cdot\mathbf{g} = \mathbf{b}$, where $\mathbf{A}$ is a $(l_M/2) \times (l_M/2)$ square matrix of elements

$$A_{ij} = \sum_{l=2}^{l_M} \sqrt{\frac{l(l+1)}{l_j(l_j+1)}}\, C(l_i, l, l_j; 0, 0, 0)C(l_i, l, l_j; 0, 1, 1)\alpha_l \tag{34}$$

where $(i,j) \geq 1$. The $l_M/2$ elements of the vector $\mathbf{b}$ are given by

$$b_j = g_0 \sum_{l=2}^{l_M} \sqrt{\frac{l(l+1)}{l_j(l_j+1)}}\, C(0, l, l_j; 0, 0, 0)C(0, l, l_j; 0, 1, 1)\alpha_l \tag{35}$$

Since angular operators do not affect the zero-order terms, a second relation between $g_0(r)$ and the remaining coefficients is still necessary to provide a complete set of equations for the Fourier coefficients. One way of obtaining this extra relation is by deriving both sides of eq 32 with respect to r and integrating over the angular variables. The result is

$$g_0(r) = 1 - \sum_{l=0}^{l_M} \frac{1}{2l+1} \int_r^\infty g_l(r') \frac{d\alpha_l(r')}{dr'}\mathrm{d}r' \tag{36}$$

where we have used the fact that $g_0(r) \to 1$ when $r \to \infty$. The above matrix form of the HNC relations can be numerically solved together

DOI: 10.1021/acsnano.7b08843
ACS Nano 2018, 12, 4321−4337

with eq 31 in order to specify the coefficients that determine the pair correlation in eq 28 in a unique way. All results in this work have been obtained by setting $l_M = 14$, corresponding to a total of 8 independent coefficients.

AUTHOR INFORMATION

Corresponding Author

*E-mail: christos.likos@univie.ac.at.

ORCID

Priti S. Mohanty: 0000-0001-8706-8005

Erik Bialik: 0000-0003-1151-4528

Peter Schurtenberger: 0000-0002-2790-8831

Christos N. Likos: 0000-0003-3550-4834

Notes

The authors declare no competing financial interest.

ACKNOWLEDGMENTS

The authors are thankful to J. Dhont and M. Rubinstein for helpful discussions. This work was supported in part by the European Training Network COLLDENSE (H2020-MCSA-ITN-2014, grant no. 642774). P.S. acknowledges financial support from the Swedish Research Council (project 2014-4037), the Knut and Alice Wallenberg Foundation (project grant KAW 2014.0052), and the European Research Council (ERC-339678-COMPASS). P.S.M. acknowledges SERB, Department of Science and Technology (ref. SB/S3/CE/042/2015) India for partial support. Computational resources from the Vienna Scientific Cluster (VSC) are gratefully acknowledged.

REFERENCES

(1) Saunders, B. R.; Vincent, B. Microgel Particles as Model Colloids: Theory, Properties and Applications. *Adv. Colloid Interface Sci.* **1999**, *80*, 1−25.

(2) Pelton, R. Temperature-Sensitive Aqueous Microgels. *Adv. Colloid Interface Sci.* **2000**, *85*, 1.

(3) Likos, C. N. Soft Matter With Soft Particles. *Soft Matter* **2006**, *2*, 478−498.

(4) *Hydrogel Micro- and Nanoparticles*; Lyon, L. A., Serpe, M. J., Eds.; Wiley VCH: Weinheim, 2012.

(5) Pelton, R.; Hoare, T. *Microgel Suspensions*; Wiley-VCH Verlag GmbH & Co. KGaA: Weinheim, 2011; pp 1−32.

(6) Grzelczak, M.; Vermant, J.; Furst, E. M.; Liz-Marzán, L. M. Directed Self-Assembly of Nanoparticles. *ACS Nano* **2010**, *4*, 3591−3605.

(7) Schurtenberger, P. *Driven self-Assembly. Proceedings of the International School of Physics "Enrico Fermi": Soft Matter Self-Assembly*; IOS Press: Amsterdam, 2016; pp 81−136.

(8) Handelman, A.; Beker, P.; Amdursky, N.; Rosenman, G. Physics and Engineering of Peptide Supramolecular Nanostructures. *Phys. Chem. Chem. Phys.* **2012**, *14*, 6391−6408.

(9) Stupp, S. I.; Zha, R. H.; Palmer, L. C.; Cui, H.; Bitton, R. Self-Assembly of Biomolecular Soft Matter. *Faraday Discuss.* **2013**, *166*, 9−30.

(10) Hill, J. P.; Shrestha, L. K.; Ishihara, S.; Ji, Q.; Ariga, K. Self-Assembly: From Amphiphiles to Chromophores and Beyond. *Molecules* **2014**, *19*, 8589−8609.

(11) McManus, J. J.; Charbonneau, P.; Zaccarelli, E.; Asherie, N. The Physics of Protein Self-Assembly. *Curr. Opin. Colloid Interface Sci.* **2016**, *22*, 73−79.

(12) Girard, M.; Millan, J. A.; Olvera de la Cruz, M. DNA-Driven Assembly: From Polyhedral Nanoparticles to Proteins. *Annu. Rev. Mater. Res.* **2017**, *47*, 33−49.

(13) Hagan, M. F. Modeling Viral Capsid Assembly. *Adv. Chem. Phys.* **2014**, *155*, 1−68.

(14) Steinmetz, N. F.; Manchester, M. *Viral nanoparticles: Tools for Materials Science and Biomedicine*; Pan Stanford Publishing Pte. Ltd.: Singapore, 2011.

(15) Samantaray, K.; Bhol, P.; Sahoo, B.; Barik, S. K.; Jathavedan, K.; Sahu, B. R.; Suar, M.; Bhat, S. K.; Mohanty, P. S. Template-Free Assembly in Living Bacterial Suspension under External Electric Field. *ACS Omega* **2017**, *2*, 1019−1024.

(16) Toor, A.; Feng, T.; Russell, T. P. Self-Assembly of Nanomaterials at Fluid Interfaces. *Eur. Phys. J. E: Soft Matter Biol. Phys.* **2016**, *39*, 57.

(17) Sun, H.; Luo, Q.; Hou, C.; Liu, J. Nanostructures Based on Protein Self-Assembly: From Hierarchical Construction to Bioinspired Materials. *Nano Today* **2017**, *14*, 16−41.

(18) Thorkelsson, K.; Bai, P.; Xu, T. Self-Assembly and Applications of Anisotropic Nanomaterials: A Review. *Nano Today* **2015**, *10*, 48−66.

(19) Sanson, N.; Rieger, J. Synthesis of Nanogels/Microgels by Conventional and Controlled Radical Crosslinking Copolymerization. *Polym. Chem.* **2010**, *1*, 965−977.

(20) Walther, A.; Müller, A. H. E. Janus Particles: Synthesis, Self-Assembly, Physical Properties, and Applications. *Chem. Rev.* **2013**, *113*, 5194−5261.

(21) Bianchi, E.; Blaak, R.; Likos, C. N. Patchy Colloids: State of the Art and Perspectives. *Phys. Chem. Chem. Phys.* **2011**, *13*, 6397−6410.

(22) Bianchi, E.; Kahl, G.; Likos, C. N. Inverse Patchy Colloids: From Microscopic Description to Mesoscopic Coarse-Graining. *Soft Matter* **2011**, *7*, 8313−8323.

(23) Novak, E. V.; Pyanzina, E. S.; Kantorovich, S. S. Behaviour of Magnetic Janus-like Colloids. *J. Phys.: Condens. Matter* **2015**, *27*, 234102.

(24) Dempster, J.; Olvera de la Cruz, M. Aggregation of Heterogeneously Charged Colloids. *ACS Nano* **2016**, *10*, 5909−15.

(25) Bradley, L. C.; Chen, W.-H.; Stebe, K. J.; Lee, D. Janus and Patchy Colloids at Fluid Interfaces. *Curr. Opin. Colloid Interface Sci.* **2017**, *30*, 25−33.

(26) Bianchi, E.; van Oostrum, P.; Likos, C. N.; Kahl, G. Inverse Patchy Colloids: Synthesis, Modeling and Self-Organization. *Curr. Opin. Colloid Interface Sci.* **2017**, *30*, 8−15.

(27) Caruso, F. Nanoengineering of Particle Surfaces. *Adv. Mater.* **2001**, *13*, 11−22.

(28) Di Michele, L.; Eiser, E. Developments in Understanding and Controlling Self Assembly of DNA-Functionalized Colloids. *Phys. Chem. Chem. Phys.* **2013**, *15*, 3115−3129.

(29) Byrom, J.; Han, P.; Savory, M.; Biswal, S. L. Directing Assembly of DNA-Coated Colloids with Magnetic Fields To Generate Rigid, Semiflexible, and Flexible Chains. *Langmuir* **2014**, *30*, 9045−9052.

(30) Pincus, P. Colloid Stabilization with Grafted Polyelectrolytes. *Macromolecules* **1991**, *24*, 2912−2919.

(31) Shenhar, R.; Norsten, T. B.; Rotello, V. M. Polymer-Mediated Nanoparticle Assembly: Structural Control and Applications. *Adv. Mater.* **2005**, *17*, 657−669.

(32) Zhou, T.; Qi, H.; Han, L.; Barbash, D.; Li, C. Y. Towards Controlled Polymer Brushes *via* a Self-Assembly-Assisted-Grafting-to Approach. *Nat. Commun.* **2016**, *7*, 11119.

(33) Chen, W.-L.; Cordero, R.; Tran, H.; Ober, C. K. 50th Anniversary Perspective: Polymer Brushes: Novel Surfaces for Future Materials. *Macromolecules* **2017**, *50*, 4089−4113.

(34) Likos, C. N. Effective Interactions in Soft Condensed Matter Systems. *Phys. Rep.* **2001**, *348*, 267−439.

(35) Likos, C. N. *Microgel Suspensions*; Wiley-VCH Verlag GmbH & Co. KGaA: Weinheim, 2011; pp 163−193.

(36) Vincent, B.; Saunders, B. *Microgel Suspensions*; Wiley-VCH Verlag GmbH & Co. KGaA: Weinheim, 2011; pp 133−162.

(37) Holmqvist, P.; Mohanty, P. S.; Nägele, G.; Schurtenberger, P.; Heinen, M. Structure and Dynamics of Loosely Cross-Linked Ionic Microgel Dispersions in the Fluid Regime. *Phys. Rev. Lett.* **2012**, *109*, 048302.

DOI: 10.1021/acsnano.7b08843
ACS Nano 2018, 12, 4321−4337

(38) Riest, J.; Athanasopoulou, L.; Egorov, S. A.; Likos, C. N.; Ziherl, P. Elasticity of Polymeric Nanocolloidal Particles. *Sci. Rep.* **2015**, *5*, 15854.
(39) Bachman, H.; Brown, A. C.; Clarke, K. C.; Dhada, K. S.; Douglas, A.; Hansen, C. E.; Herman, E.; Hyatt, J. S.; Kodlekere, P.; Meng, Z.; et al. Ultrasoft, Highly Deformable Microgels. *Soft Matter* **2015**, *11*, 2018−2028.
(40) Urich, M.; Denton, A. R. Swelling, Structure, and Phase Stability of Compressible Microgels. *Soft Matter* **2016**, *12*, 9086−9094.
(41) Ben-Naim, A. Solvent-Induced Interactions: Hydrophobic and Hydrophilic Phenomena. *J. Chem. Phys.* **1989**, *90*, 7412−7425.
(42) Ben-Naim, A. On the Driving Forces for Protein-Protein Association. *J. Chem. Phys.* **2006**, *125*, 024901.
(43) Tan, B. H.; Tam, K. C. Review on the Dynamics and Micro-Structure of pH-Responsive Nano-Colloidal Systems. *Adv. Colloid Interface Sci.* **2008**, *136*, 25−44.
(44) dos Santos, A. P.; Girotto, M.; Levin, Y. Simulations of Polyelectrolyte Adsorption to a Dielectric Like-Charged Surface. *J. Phys. Chem. B* **2016**, *120*, 10387−10393.
(45) Durell, S. R.; Ben-Naim, A. Hydrophobic-Hydrophilic Forces in Protein Folding. *Biopolymers* **2017**, *107*, e23020.
(46) Tergolina, V. B.; dos Santos, A. P. Effect of Dielectric Discontinuity on a Spherical Polyelectrolyte Brush. *J. Chem. Phys.* **2017**, *147*, 114103.
(47) Levin, Y. Electrostatic Correlations: From Plasma to Biology. *Rep. Prog. Phys.* **2002**, *65*, 1577.
(48) Messina, R. Electrostatics in Soft Matter. *J. Phys.: Condens. Matter* **2009**, *21*, 113102.
(49) Denton, A. R. In *Nanostructured Soft Matter: Experiment, Theory, Simulation and Perspectives*; Zvelindovsky, A. V., Ed.; Springer Netherlands: Dordrecht, 2007; pp 395−433.
(50) Saunders, B. R.; Laajam, N.; Daly, E.; Teow, S.; Hu, X.; Stepto, R. Microgels: From Responsive Polymer Colloids to Biomaterials. *Adv. Colloid Interface Sci.* **2009**, *147*−*148*, 251−262.
(51) Crassous, J.; Mihut, A.; Månsson, L.; Schurtenberger, P. Anisotropic Responsive Microgels with Tuneable Shape and Interactions. *Nanoscale* **2015**, *7*, 15971−15982.
(52) Levin, Y.; Diehl, A.; Fernández-Nieves, A.; Fernández-Barbero, A. Thermodynamics of Ionic Microgels. *Phys. Rev. E: Stat. Phys., Plasmas, Fluids, Relat. Interdiscip. Top.* **2002**, *65*, 036143.
(53) Colla, T.; Likos, C. N.; Levin, Y. Equilibrium Properties of Charged Microgels: A Poisson-Boltzmann-Flory Approach. *J. Chem. Phys.* **2014**, *141*, 234902.
(54) Adroher-Benítez, I.; Ahualli, S.; Martín-Molina, A.; Quesada-Pérez, M.; Moncho-Jordá, A. Role of Steric Interactions on the Ionic Permeation Inside Charged Microgels: Theory and Simulations. *Macromolecules* **2015**, *48*, 4645−4656.
(55) Denton, A. R.; Tang, Q. Counterion-Induced Swelling of Ionic Microgels. *J. Chem. Phys.* **2016**, *145*, 164901.
(56) Rizzi, L. G.; Levin, Y. Influence of Network Topology on the Swelling of Polyelectrolyte Nanogels. *J. Chem. Phys.* **2016**, *144*, 114903.
(57) Adroher-Benitez, I.; Martin-Molina, A.; Ahualli, S.; Quesada-Perez, M.; Odriozola, G.; Moncho-Jordá, A. Competition Between Excluded-Volume and Electrostatic Interactions for Nanogel Swelling: Effects of the Counterion Valence and Nanogel Charge. *Phys. Chem. Chem. Phys.* **2017**, *19*, 6838−6848.
(58) Riest, J.; Mohanty, P.; Schurtenberger, P.; Likos, C. N. Coarse-Graining of Ionic Microgels: Theory and Experiment. *Z. Phys. Chem.* **2012**, *226*, 711−735.
(59) Seuss, M.; Schmolke, W.; Drechsler, A.; Fery, A.; Seiffert, S. Core-Shell Microgels with Switchable Elasticity at Constant Interfacial Interaction. *ACS Appl. Mater. Interfaces* **2016**, *8*, 16317−16327.
(60) de Aguiar, I. B.; van de Laar, T.; Meireles, M.; Bouchoux, A.; Sprakel, J.; Schroën, K. Deswelling and Deformation of Microgels in Concentrated Packings. *Sci. Rep.* **2017**, *7*, 10223.
(61) Mohanty, P. S.; Bagheri, P.; Yethiraj, A.; Schurtenberger, P. Deformable Particles with Anisotropic Interactions: Unusual Field-Induced Structural Transitions in Ultrasoft Ionic Microgel Colloids. *Soft Matter* **2012**, *8*, 10819−10822.
(62) van Blaaderen, A.; Dijkstra, M.; van Roij, R.; Imhof, A.; Kamp, M.; Kwaadgras, B. W.; Vissers, T.; Liu, B. Manipulating the Self Assembly of Colloids in Electric Fields. *Eur. Phys. J.: Spec. Top.* **2013**, *222*, 2895−2909.
(63) Löwen, H. Introduction to Colloidal Dispersions in External Fields. *Eur. Phys. J.: Spec. Top.* **2013**, *222*, 2727−2737.
(64) Nöjd, S.; Mohanty, P. S.; Bagheri, P.; Yethiraj, A.; Schurtenberger, P. Electric Field Driven Self-Assembly of Ionic Microgels. *Soft Matter* **2013**, *9*, 9199.
(65) Mohanty, P. S.; Bagheri, P.; Nöjd, S.; Yethiraj, A.; Schurtenberger, P. Multiple Path-Dependent Routes for Phase-Transition Kinetics in Thermoresponsive and Field-Responsive Ultrasoft Colloids. *Phys. Rev. X* **2015**, *5*, 011030.
(66) Osterman, N.; Poberaj, I.; Dobnikar, J.; Frenkel, D.; Ziherl, P.; Babić, D. Field-Induced Self-Assembly of Suspended Colloidal Membranes. *Phys. Rev. Lett.* **2009**, *103*, 228301.
(67) Ray, A.; Fischer, T. M. Magnetic Field Controlled Composite Paramagnetic-Diamagnetic Colloidal Phases. *J. Phys. Chem. B* **2012**, *116*, 8233.
(68) Andreu, J. S.; Camacho, J.; Faraudo, J. Aggregation of Superparamagnetic Colloids in Magnetic Fields: The Quest for the Equilibrium State. *Soft Matter* **2011**, *7*, 2336.
(69) Crassous, J.; Mihut, A.; Wernersson, E.; Pfleiderer, P.; Vermant, J.; Linse, P.; Schurtenberger, P. Field-Induced Assembly of Colloidal Ellipsoids into Well-Defined Microtubules. *Nat. Commun.* **2014**, *5*, 5516.
(70) Tang, Y.; Chen, Q. W.; Chen, R. Magnetic Field Induced Controllable Self-Assembly of Maghemite Nanocrystals: From 3d Arrays to 1d Nanochains. *Appl. Surf. Sci.* **2015**, *347*, 202−207.
(71) Martchenko, I.; Crassous, J. J.; Mihut, A. M.; Bialik, E.; Hirt, A. M.; Rufier, C.; Menzel, A.; Dietsch, H.; Linse, P.; Schurtenberger, P. Anisotropic Magnetic Particles in a Magnetic Field. *Soft Matter* **2016**, *12*, 8755.
(72) Malik, V.; Pal, A.; Pravaz, O.; Crassous, J. J.; Garnville, S.; Grobety, B.; Hirt, A. M.; Dietsch, H.; Schurtenberger, P. Hybrid Magnetic Iron Oxide Nanoparticles with Tunable Field-Directed Self-Assembly. *Nanoscale* **2017**, *9*, 14405−14413.
(73) Mohanty, P. S.; Nöjd, S.; Bergman, M. J.; Nägele, G.; Arrese-Igor, S.; Alegria, A.; Roa, R.; Schurtenberger, P.; Dhont, J. K. G. Dielectric Spectroscopy of Ionic Microgel Suspensions. *Soft Matter* **2016**, *12*, 9705−9727.
(74) McMillan, W. G., Jr.; Mayer, J. E. The Statistical Thermodynamics of Multicomponent Systems. *J. Chem. Phys.* **1945**, *13*, 276−305.
(75) Uppapalli, S.; Zhao, H. Polarization of a Diffuse Soft Particle Subjected to an Alternating Current Field. *Langmuir* **2012**, *28*, 11164−11172.
(76) de Gennes, P.; Pincus, P. Pair Correlations in a Ferromagnetic Colloid. *Eur. Phys. J. B* **1970**, *11*, 189−198.
(77) Zubarev, A. Yu; Iskakova, L. Yu. Theory of Physical Properties of Magnetic Liquids with Chain Aggregates. *JETP* **1995**, *80*, 857−866.
(78) Zubarev, A. Y.; Iskakova, L. Y. Effect of Chainlike Aggregates on Dynamical Properties of Magnetic Liquids. *Phys. Rev. E: Stat. Phys., Plasmas, Fluids, Relat. Interdiscip. Top.* **2000**, *61*, 5415−5421.
(79) Mendelev, V.; Ivanov, A. Ferrofluid Aggregation in Chains Under the Influence of a Magnetic Field. *Phys. Rev. E* **2004**, *70*, 051502.
(80) Kantorovich, S.; Ivanov, A.; Rovigatti, L.; Tavares, J.; Sciortino, F. Nonmonotonic Magnetic Susceptibility of Dipolar Hard-Spheres at Low Temperature and Density. *Phys. Rev. Lett.* **2013**, *110*, 148306.
(81) Ivanov, A.; Kantorovich, S. Chain Aggregate Structure and Magnetic Birefringence in Polydisperse Ferrofluids. *Phys. Rev. E: Stat. Phys., Plasmas, Fluids, Relat. Interdiscip. Top.* **2004**, *70*, 021401.
(82) Holm, C.; Ivanov, A.; Kantorovich, S.; Pyanzina, E.; Reznikov, E. Equilibrium Properties of a Bidisperse Ferrofluid with Chain Aggregates: Theory and Computer Simulations. *J. Phys.: Condens. Matter* **2006**, *18*, S2737−S2756.

DOI: 10.1021/acsnano.7b08843
ACS Nano 2018, 12, 4321−4337

(83) Smallenburg, F.; Vutukuri, H. R.; Imhof, A.; et al. Self-Assembly of Colloidal Particles into Strings in a Homogeneous External Electric or Magnetic Field. *J. Phys.: Condens. Matter* **2012**, *24*, 464113.
(84) Grosse, C.; Shilov, V. N. Theory of the Low-Frequency Electrorotation of Polystyrene Particles in Electrolyte Solution. *J. Phys. Chem.* **1996**, *100*, 1771−1778.
(85) Hoffmann, N.; Likos, C. N.; Hansen, J.-P. Linear Screening of the Electrostatic Potential around Spherical Particles with Non-Spherical Charge Patterns. *Mol. Phys.* **2004**, *102*, 857−868.
(86) Mohanty, P. S.; Nöjd, S.; van Gruijthuijsen, K.; Crassous, J. J.; Obiols-Rabassa, M.; Schweins, R.; Stradner, A.; Schurtenberger, P. Interpenetration of Polymeric Microgels at Ultrahigh Densities. *Sci. Rep.* **2017**, *7*, 1487.
(87) Denton, A. Counterion Penetration and Effective Electrostatic Interactions in Solutions of Polyelectrolyte Stars and Microgels. *Phys. Rev. E: Stat. Phys., Plasmas, Fluids, Relat. Interdiscip. Top.* **2003**, *67*, 011804.
(88) Colla, T.; Likos, C. N. Effective Interactions in Polydisperse Systems of Penetrable Macroions. *Mol. Phys.* **2015**, *113*, 2496−2510.
(89) Mohanty, P. S.; Paloli, D.; Crassous, J. J.; Zaccarelli, E.; Schurtenberger, P. Effective Interactions Between Soft-Repulsive Colloids: Experiments, Theory, and Simulations. *J. Chem. Phys.* **2014**, *140*, 094901.
(90) Girotto, M.; dos Santos, A. P.; Colla, T.; Levin, Y. Yukawa Particles in a Confining Potential. *J. Chem. Phys.* **2014**, *141*, 014106.
(91) Romeo, G.; Imperiali, L.; Kim, J. W.; Fernández-Nieves, A.; Weitz, D. A. Origin of De-Swelling and Dynamics of Dense Ionic Microgel Suspensions. *J. Chem. Phys.* **2012**, *136*, 124905.
(92) Pelaez-Fernández, M.; Souslov, A.; Lyon, L. A.; Goldbart, P. M.; Fernández-Nieves, A. Impact of Single-Particle Compressibility on the Fluid-Solid Phase Transition for Ionic Microgel Suspensions. *Phys. Rev. Lett.* **2015**, *114*, 098303.
(93) Sherman, Z. M.; Rosenthal, H.; Swan, J. W. Phase Separation Kinetics of Dynamically Self-Assembling Nanoparticles with Toggled Interactions. *Langmuir* **2018**, *34*, 1029−1041.
(94) Halsey, T.; Toor, W. Structure of Electrorheological Fluids. *Phys. Rev. Lett.* **1990**, *65*, 2820.
(95) Blum, L.; Torruella, A. J. Invariant Expansion for Two-Body Correlations: Thermodynamic Functions, Scattering, and the Orstein-Zernike Equation. *J. Chem. Phys.* **1972**, *56*, 303−310.
(96) Blum, L. Invariant Expansion II. The Orstein-Zernike Equation for Nonspherical Molecules and an Extended Solution to the Mean Spherical Model. *J. Chem. Phys.* **1972**, *57*, 1862−1869.
(97) Blum, L. Invariant expansion III: The General Solution of the Mean Spherical Model for Neutral Spheres with Electostatic Interactions. *J. Chem. Phys.* **1973**, *58*, 3295−3303.
(98) Fries, P. H.; Patey, G. The Solution of the Hypernetted Chain Approximation for Fluids of Nonspherical Particles. A General Method with Application to Dipolar Hard Spheres. *J. Chem. Phys.* **1985**, *82*, 429−440.
(99) Dhont, J. K. G. The Static Structure Factor for Fully Aligned Charged Rod-Like Macromolecules. *J. Chem. Phys.* **1986**, *85*, 5983−5990.
(100) Klapp, S.; Forstmann, F. Phase Behavior of Aligned Dipolar Hard Spheres: Integral Equations and Density Functional Results. *Phys. Rev. E: Stat. Phys., Plasmas, Fluids, Relat. Interdiscip. Top.* **1999**, *60*, 3183−3198.
(101) Brandt, P. C.; Ivlev, A. V.; Morfill, G. E. String-Fluid Transition in Systems with Aligned Anisotropic Interactions. *J. Chem. Phys.* **2010**, *132*, 234709.
(102) Crocker, J. C.; Grier, D. G. Methods of Digital Video Microscopy for Colloidal Studies. *J. Colloid Interface Sci.* **1996**, *179*, 298−310.
(103) Nymand, T. M.; Linse, P. Ewald Summation and Reaction Field Methods for Potentials with Atomic Charges, Dipoles, and Polarizabilities. *J. Chem. Phys.* **2000**, *112*, 6152−6160.

DOI: 10.1021/acsnano.7b08843
ACS Nano 2018, 12, 4321−4337